Nature Communications

https://doi.org/10.1038/s41467-026-69951-7

Article in Press

Structural and functional implications of phase separation of membrane protein LacY in *Escherichia coli*

Received: 7 May 2025

Accepted: 13 February 2026

Cite this article as: Linnik, D., Sultanji, S., Stevens, J.A. *et al.* Structural and functional implications of phase separation of membrane protein LacY in *Escherichia coli*. *Nat Commun* (2026). https://doi.org/10.1038/s41467-026-69951-7

Dmitrii Linnik, Sumayra Sultanji, Jan A. Stevens, Gea K. Schuurman-Wolters, Rinse de Boer, Christiaan M. Punter, Siewert J. Marrink, Ivan Maslov & Bert Poolman

Structural and functional implications of phase separation of membrane protein LacY in *Escherichia coli*

*Dmitrii Linnik[1], Sumayra Sultanji[1], Jan A. Stevens[2], Gea K. Schuurman-Wolters[1], Rinse de Boer[3], Christiaan M. Punter[1], Siewert J. Marrink[2], Ivan Maslov[1], and Bert Poolman[1]**

[1]Department of Biochemistry, Groningen Biomolecular Sciences & Biotechnology Institute, University of Groningen, Nijenborgh 3, 9747 AG Groningen, the Netherlands.

[2]Molecular Dynamics Group, Groningen Biomolecular Sciences and Biotechnology Institute, University of Groningen, Nijenborgh 7, 9747 AG Groningen, the Netherlands

[3]Molecular Immunology, Groningen Biomolecular Sciences & Biotechnology Institute, University of Groningen, Nijenborgh 7, 9747 AG Groningen, The Netherlands

* E.mail: b.poolman@rug.nl

Abstract

Liquid-liquid phase-separation (LLPS) controls protein activity and dynamically organizes (macro)molecules in living systems without the need for membrane-bound compartments. Biomolecular condensates of water-soluble proteins have extensively been studied, but little is known about LLPS of membrane proteins. In this work we induce *in vivo* condensation of lactose permease (LacY), a widely-studied model monomeric inner membrane protein in *Escherichia coli*, and evaluate how it affects LacY function. We fused LacY with engineered, condensate-forming protein PopTag. We observe major changes in the localization and mobility of $LacY^{Pop}$. Molecular dynamics simulations show how the PopTag domain drives the condensate-like association dynamics of $LacY^{Pop}$ through hydrophobic sticker interactions. $LacY^{Pop}$ preserves native-level transport activity and outperforms the non-condensed LacY under mild hyperosmotic stress (osmotic upshift). In osmotically stressed cells, membrane-bound biomolecular condensates also reduce deformation of the cytoplasmic membrane. Perturbation experiments suggest that membrane curvature drives the accumulation of $LacY^{Pop}$ at the poles of *E. coli*. Co-condensation of LacY and β-galactosidase LacZ slightly reduces their activity and results in remarkable cellular reorganization of the proteins. Our research shows the localization, dynamics, and function of phase-separated membrane proteins in bacteria and highlights the potential of LLPS for engineering complex metabolic networks *in vivo*.

Introduction

Phase separation of biomolecules is an emerging field of cell biology[1,2]. Numerous examples of liquid-liquid phase separation (LLPS) have been discovered in eukaryotic cells (e.g. nucleoli, Cajal bodies, stress granules, U-bodies etc.[3]). The physico-chemical properties of condensates, such as viscosity, pH, oxygen concentration and molecular composition, can differ from the surrounding milieu, favoring or disfavoring certain reactions and interactions[4]. The propensity of a molecule to partition in a condensate relative to the surrounding medium typically also differs. Formation of biomolecular condensates of protein and/or nucleic acids is governed by attractive intermolecular interactions between motifs in intrinsically disordered regions (IDR), the so-called stickers-and-spacers framework, or repeats of folded domains with connecting linkers[5]. The ability of a macromolecule to interact with multiple partners simultaneously (multivalency) is a requirement for phase separation[6].

The fraction of water-soluble proteins with IDRs is 30-40% in mammalian cells but thought to be lower in bacteria[3]. A subfraction of these molecules enable multivalent interactions that drive biomolecular condensation. Little is known of phase-separation of transmembrane proteins driven by intermolecular protein interactions. Some examples are T-cell receptors in mammalian cells, Rv1747 protein in *Mycobacterium tuberculosis,* and PodJ in *Caulobacter vibrioides.* The phase separation of T-cell receptors and their auxiliary proteins plays a role in the transduction of signals within the immune system[7]. The phase separation and 2D clustering of the ATP-binding cassette transporter Rv1747 is promoted by condensation of two 2-Forkhead-associated cytosolic domains linked by an IDR and tuned by phosphorylation[8]. In PodJ protein part of the cytosolic coiled-coil domain and IDR are responsible for the condensate formation[9]. We note that IDRs are present in numerous types of membrane proteins and often implicated in their regulation, but they are generally not seen as possibility for condensation of the proteins and putative multivalency effects have not been explored[10–12]. Next to protein-driven phase separation, membrane proteins can be organized via scaffolding proteins like flotillins[13,14] or partition differentially in liquid-disordered and liquid-ordered lipid domains in the membrane[15], but these mechanisms are not relevant for this study.

Biomolecular condensates of water-soluble proteins can physically associate with the lipid bilayer but they are not inserted into the membrane[16]. Such condensates are generally composed of proteins, often with intrinsically disordered regions, and/or nucleic acids, enabling multivalent interactions that drive condensate formation. Membrane association can occur through electrostatic interactions, lipid-binding domains, or curvature-sensing motifs, leading to surface wetting, local membrane deformation, and curvature remodeling. This type of membrane-condensate interaction can remodel membrane morphology through capillary forces, induce nanoscale ruffling at the condensate–membrane interface, and couple protein phase separation to lipid phase behavior. Such condensates are attributed important biological roles, including

spatial regulation of signaling pathways, organization of cytoskeletal elements, facilitation of endocytic events, and remodeling of organelle surfaces.

To study the mechanisms and implications of multivalent site-specific interactions between soluble regions of membrane proteins *in vivo*, we use the condensation domain PopTag to drive phase separation of an integral membrane protein. PopTag is the C-terminal part of the phase separating protein PopZ, which is important for the asymmetrical division of *Caulobacter vibrioides*[17,18]. PopTag consists of three sticker sequences separated by IDRs, allowing multivalent interactions and thus condensate formation. We fused this protein tag to the C-terminus of lactose permease LacY of *Escherichia coli*. LacY natively lacks intrinsically disordered regions (IDRs), it does not undergo phase separation and is homogenously distributed in the inner membrane. *E. coli* lacks PopZ orthologues, therefore introduction of PopTag should be orthogonal to native phase-separating systems. Our synthetic system of a polytopic membrane protein fused to a condensation-driving domain mimics features widely present in transmembrane proteins and can serve as platform to investigate structural and functional implications of LLPS of membrane proteins[10,19].

Addition of PopTag to LacY results in a predominantly polar localization of the fusion protein. We show the condensate-like behavior of $LacY^{Pop}$ fused to a fluorescent protein mEos3.2 ($LacY^{mEos\text{-}Pop}$, Supplementary Table 1) by fluorescence recovery after photobleaching (FRAP), photoactivated localization microscopy (PALM), and single-molecule displacement mapping (SMdM). Using coarse-grained molecular dynamics simulations, we show how the PopTag domains bridge LacY proteins through hydrophobic sticker interactions and form a dynamic network of protein-protein associations leading to condensate formation. In a series of perturbation experiments we show that nucleoid exclusion is not critical for the polar localization, while local membrane curvature plays a role. Using ^{14}C-lactose transport experiments, we show that LacY is fully active in condensates and even outperforms native LacY. Finally, we designed and characterized heterocondensates of $LacY^{Pop}$ with its downstream lactose-metabolizing enzyme, β-galactosidase (LacZ)-PopTag ($LacZ^{Pop)}$.

Results

PopTag induces biomolecular condensation of LacY in the inner membrane of *E. coli*

Genes for LacY-mEos3.2 and LacY-mEos3.2-PopTag fusions were inserted in the pBAD vector and transformed into *E. coli* BW25113, resulting in BW25113 $LacY^{mEos}$ and BW25113 $LacY^{mEos\text{-}Pop}$. Wide-field fluorescence microscopy shows that $LacY^{mEos}$ is equally distributed in the inner membrane, without preferred localization, whereas $LacY^{mEos\text{-}Pop}$ is predominantly present at the cell poles but discrete foci are also visible at the lateral membrane (Figure 1a). To reveal

fine details of LacY$^{mEos\text{-}Pop}$ clusters we performed PALM microscopy with live cells and cells fixed with formaldehyde-glutaraldehyde (4% w/v formaldehyde, 0.4% w/v glutaraldehyde in 100 mM sucrose dissolved in MQ water) (Figure 1b). In live cells, single-molecule localizations, recorded for 30 min (~100.000 frames), show patterns akin those of the wide-field fluorescence microscopy images, whereas reconstructions recorded for 6 min (~20.000 frames) reveal multiple clusters on the lateral membrane, similar to what has been seen for Rv1747 in *M. tuberculosis*[8]. The fraction of localizations at the cell poles is two times higher for LacY$^{mEos\text{-}Pop}$ (0.62 ± 0.06) than for LacY^{mEos} (0.30 ± 0.04) (Figure 1c). In fixed cells, the localization of LacY$^{mEos\text{-}Pop}$ is preserved, but the apparent size of the clusters is smaller, presumably due to reduction of the "motion blur" (Supplementary Video 1). The difference in cluster size observed in PALM reconstructions reflects the physical size of the clusters and is not due to a different localization precision, which is similar for live (25±13 nm) and fixed (24±13 nm) BW25113 LacY$^{mEos\text{-}Pop}$ cells. Thus, LacY$^{mEos\text{-}Pop}$ predominantly localizes at cell poles and forms mobile foci in the lateral membrane that become immobile upon fixation.

To investigate the mobility of LacY^{mEos} and LacY$^{mEos\text{-}Pop}$, we performed fluorescence recovery after photobleaching (FRAP) and single-molecule displacement mapping (SMdM[20–22]) experiments. The fluorescence recovery of LacY$^{mEos\text{-}Pop}$ had a half-time of 134 ± 47 sec seconds and reached ~14% of the initial fluorescence, and the majority of the molecules partition inside punctuated condensates upon recovery (Figure 1d and Supplementary Figure 1). Non-condensed LacY^{mEos} recovered with a half-time of 0.61 ± 0.14 sec and reached ~72% of the initial fluorescence (Figure 1e). The moderate recovery of LacY$^{mEos\text{-}Pop}$ reflects protein exchange between the biomolecular condensate at the bleached pole and the lateral membrane (small fraction of total LacY$^{mEos\text{-}Pop}$); the fluorescence of the non-bleached pole does not change during the recovery phase. Photobleaching of the lateral membrane did not result in fluorescence recovery, indicating that LacY^{Pop} is tightly sequestered within the polar condensates. The recovery at the poles is not due to reactivation of the fluorescent protein, because we saw no recovery of fluorescence when cells were fully photobleached (Figure 1d). Furthermore, the fluorescence recovery at the poles is not caused by synthesis of new protein, because the recovery was similar in untreated and translation inhibitor (chloramphenicol)-treated cells.

Next, we examined the mobility of individual LacY^{mEos} and LacY$^{mEos\text{-}Pop}$ molecules with SMdM[23] (Figure 1f). The apparent diffusion coefficient (*D*) of LacY^{mEos} is lower at the cell poles compared to the lateral membrane (*D* = 0.17 ± 0.04 $\mu m^2/s$ versus 0.22 ± 0.06 $\mu m^2/s$, two-sided t-test p-value = 0.0002) (Figure 1g). This decrease in *D* suggests a lower protein mobility at the cell poles but can also be a result of two-dimensional projection of protein movement across the membrane. The apparent diffusion coefficient of LacY$^{mEos\text{-}Pop}$ is similar between the cell poles and the lateral membrane (*D* = 0.11 ± 0.02 $\mu m^2/s$ vs 0.12 ± 0.01 $\mu m^2/s$, two-sided t-test p-value = 0.34) and is 35% lower than that of polar LacY^{mEos}. Since LacY$^{mEos\text{-}Pop}$ mobility in the lateral membrane and at the cell pole is reduced to a similar extent, we conclude that LacY$^{mEos\text{-}Pop}$ forms

not only large condensates at the cell poles, but also smaller condensates in the lateral membrane.

We performed transmission electron microscopy on cryo-fixed BW25113 LacY^{mEos} and BW25113 LacY$^{mEos\text{-}Pop}$ cells to verify the membrane localization of LacY$^{mEos\text{-}Pop}$ condensates at higher resolution than observed by light microscopy. We observe electron-dense regions on the cytoplasmic face of the inner membrane at the cell pole in 4 out of 6 BW25113 LacY$^{mEos\text{-}Pop}$ cells and in 2 out of 10 BW25113 LacY^{mEos} cells (Figure 1h, Supplementary Figure 3). The approximate thickness of these regions is 10 nm, which is similar to the predicted length of the mEos3.2-PopTag part of LacY$^{mEos\text{-}Pop}$. Remarkably, the shape and integrity of the inner membrane adjacent to the electron-dense regions at the cell poles are preserved. These data suggest that LacY$^{mEos\text{-}Pop}$ condensates anchor to the inner membrane without deforming it. Collectively, our observations suggest that LacY$^{mEos\text{-}Pop}$ forms two-dimensional biomolecular condensates in the inner membrane of *E. coli*, with large condensates at the cell poles and smaller ones in the lateral membrane.

Hydrophobic stickers drive LacY^{Pop} condensation

To investigate how the fused PopTag influences the organization of LacY in the membrane, we performed coarse-grained molecular dynamics (MD) simulations of nine LacY proteins in an *E. coli*-like lipid membrane, with and without a PopTag (Figure 2a). The simulations were executed in triplicate for better statistics on our observations. The proteins were initially positioned in equally spaced grid configurations. During a 50 µs simulation, both proteins show a clear difference in clustering behavior. LacY proteins without a PopTag formed relatively static small clusters, maintaining approximately three separate clusters throughout the simulation. In contrast, LacY^{Pop} proteins show substantially more dynamic interactions, ultimately forming one large cluster during the simulations. Quantitative analysis confirms this difference in clustering dynamics (Figure 2d and Supplementary Figure 4), with LacY^{Pop} having more fluctuations in the number of protein-protein interactions, indicating the dynamic nature of the formed contacts.

To understand the molecular mechanism behind the PopTag-mediated clustering, we analyzed the specific residue contacts involved in PopTag-PopTag interactions. First, we performed simulations of the PopTag alone (Figure 2b). The contact map analysis reveals that inter-PopTag interactions in condensates are primarily driven by helix 1 (residues 14-31) and helix 2 (residues 40-58), with notable contacts also observed in the H1-H2 linker region (Figure 2c, right panel). We then determined the contacts formed by PopTag when fused to LacY in the membrane and find again that H1 and H2 are the primary drivers of inter-PopTag interactions (Figure 2c, left panel). The interaction interface in both cases is dominated by the amphipathic α-helices with high hydrophobic moment. The hydrophobic faces of these putative helices most likely form the "stickers" for condensation, as indicated by the hydrophobicity profile along the residue index. Contacts in the H1-H2 linker region also result from hydrophobic residue interactions, and these are enhanced in the LacY^{Pop} system due to the antiparallel binding of the PopTags. Our MD

simulations thus show that the hydrophobic character of the PopTag is important for its self-association properties.

The PopTag helices embed at the membrane surface due to their amphipathic nature, creating membrane-mediated PopTag-PopTag interactions (Figure 2a). This membrane interaction potentially competes with the solution-mediated condensate formation, as hydrophobic residues engaged with the membrane are unavailable for PopTag-PopTag interactions. It is feasible that a dynamic equilibrium exists between membrane-mediated and solution-mediated condensate formation. To explore this, we performed additional simulations of $LacY^{Pop}$ where proteins were configured at high concentration with the PopTags extended into the solvent (Supplementary Figure 6). This indeed reduced membrane association and allowed more extensive PopTag-PopTag interactions and network formation through association of the helical parts. We thus propose a two-step process for the condensate formation of $LacY^{Pop}$: Initially, PopTags interact with the membrane while exploring protein-protein contacts (Fig 2a). As the local concentration increases, protein-protein interactions dominate over membrane association, leading to PopTags interacting in solution (Supplementary Figure 6).

Together, our simulations demonstrate that the PopTags mediate interactions between otherwise non-associating LacY proteins through their hydrophobic interfaces. This creates a dynamic network of protein-protein interactions that drives the condensate-like behavior of $LacY^{Pop}$ membrane proteins.

Membrane curvature impacts distribution of LacY condensates

What determines the predominant polar localization of phase-separated LacY-mEos3.2-PopTag? We tested whether the nucleoid would exclude the condensates from the lateral membrane. We imaged BW25113 $LacY^{mEos}$ and BW25113 $LacY^{mEos\text{-}Pop}$ cells after treatment with cephalexin for four and seven hours (Figure 3ab). Cephalexin leads to elongation of *E. coli* and accumulation of multiple nucleoids in one cell[24]. After 4-hour cephalexin treatment we observed cells with two nucleoids per cell, using DAPI as a DNA-staining dye. $LacY^{mEos}$ is homogeneously distributed in the membrane, while $LacY^{mEos\text{-}Pop}$ has the same distribution as in untreated cells: the majority of the condensates are at the cell poles but some smaller foci are found at the lateral membrane. After 7-hour cephalexin treatment, the number of nucleoids per cell increased, but for both LacY variants the localization patterns remain, with the majority of $LacY^{mEos\text{-}Pop}$ at the poles and $LacY^{mEos}$ homogenously distributed. Importantly, we do not observe accumulation of $LacY^{mEos\text{-}Pop}$ in the inter-nucleoid regions, suggesting that $LacY^{mEos\text{-}Pop}$ localization is not governed by nucleoid exclusion.

To further investigate the role of the nucleoid in $LacY^{mEos\text{-}Pop}$ positioning, we visualized $LacY^{mEos\text{-}Pop}$ in nucleoid-free *E. coli* LY177 cells, where arabinose-induced expression of *I-SceI* endonuclease leads to nucleoid degradation[25], which was confirmed by DAPI staining (Figure 3c). Upon nucleoid degradation, $LacY^{mEos\text{-}Pop}$ is mostly in the polar regions with some foci on the lateral membrane, while $LacY^{mEos}$ remains homogenously distributed over the membrane. These

experiments rule out that nucleoid exclusion causes polar location of the LacY$^{mEos\text{-}Pop}$ membrane condensates.

Next, we evaluated the effect of membrane curvature on the localization of the proteins, using spheroplasts (spherical, osmotically-sensitive cells made by removing part of the outer membrane and peptidoglycan layer) prepared from BW25113 LacY^{mEos} and BW25113 LacY$^{mEos\text{-}Pop}$ cells (Figure 3d)[26,27]. Spheroplasts made from BW25113 LacY^{mEos} served as control and show homogenous LacY^{mEos} distribution. Spheroplasts from BW25113 LacY$^{mEos\text{-}Pop}$ show a variety of LacY-mEos3.2-PopTag distributions, ranging from multiple clusters per spheroplasts to almost homogeneous protein distribution. We then measured the same cells 30 min after spheroplasts formation and find a dissolution of LacY$^{mEos\text{-}Pop}$ condensates from the original poles, and the cell shape change is associated with a more homogenous localization pattern.

To capture the redistribution of LacY$^{mEos\text{-}Pop}$ upon spheroplast formation over time, we immobilized *E. coli* cells with agarose pads, supplemented with the "cocktail" for spheroplasts formation to trigger the shape change. The time-lapse videos clearly show the gradual redistribution of large phase-separated condensates from distinct foci to homogeneously localized protein over approximately 40 min (Supplementary Video 2). Thus, the loss of pole localization of phase-separated membrane-bound condensates coincides with the loss of the pole curvature. To reintroduce curvature in spheroplasts with homogeneously distributed LacY$^{mEos\text{-}Pop}$, we induced plasmolysis of the spheroplasts immobilized under agarose pads supplemented with 0.5 M NaCl. The LacY$^{mEos\text{-}Pop}$ distribution was monitored by wide-field fluorescence microscopy (Figure 3e). Remarkably, upon plasmolysis, LacY$^{mEos\text{-}Pop}$ condensates are no longer homogenously distributed in the spheroplasts but predominantly localize at highly curved, concave membrane regions (Supplementary Figure 7). Spearman correlation coefficient between the normalized curvature and normalized fluorescence intensity along deformed spheroplasts contour is 0.24, p-value <0.0001. These observations highlight the importance of membrane curvature in the spatial distribution of LacY$^{mEos\text{-}Pop}$.

Activity of condensed LacY

To evaluate the effect of condensation on LacY transport activity, we used ^{14}C-lactose and determined the uptake of the subsrate by LacY^{mEos} and LacY$^{mEos\text{-}Pop}$ in *E. coli* BW25113 *ΔlacY* (Figure 4a). The cells producing LacY$^{mEos\text{-}Pop}$ import slightly more lactose compared to the cells with LacY^{mEos}, which is seen as higher plateauing levels of the uptake curves (U_{MAX} = 2.96±0.17 versus 2.48±0.10 $\mathrm{nmol\ lactose/mg\ total\ cell\ protein}$, extra sum-of-squares F-test p-value = 0.0145, Figure 4b). The expression levels of the LacY variants are similar as determined by fluorescence analysis of cell lysates, for which the proteins were separated by SDS-PAGE. We measured 3.5 ± 0.4 x 10^3 LacY^{mEos} and 3.4 ± 0.5 x 10^3 LacY$^{mEos\text{-}Pop}$ proteins per *E. coli* cell (Supplementary Figure 8). Quantification of LacY^{mEos} and LacY$^{mEos\text{-}Pop}$ by in-gel fluorescence show

that they do not greatly exceed the native-level expression, which is ~2500 LacY molecules per cell in the fully induced state[28].

Further, we tested whether LacY condensation can rescue the decrease of activity under stress conditions, i.e. hyperosmotic stress[29]. We measured ^{14}C-lactose uptake of cells without stress and upon an increase of NaCl concentration of 160 mM or 320 mM, resulting in 2- or 3-fold increase in osmolarity (Figure 4c). Under the higher osmolarity, the maximum levels of lactose uptake U_{MAX} reduce both for BW25113 *ΔlacY* LacY^{mEos} and BW25113 *ΔlacY* LacY$^{mEos\text{-}Pop}$ cells (Figure 4d). Remarkably, under all measured conditions, LacY$^{mEos\text{-}Pop}$ outperforms LacY^{mEos}.

We then visualized the protein distribution in osmotically stressed BW25113 *ΔlacY* LacY^{mEos} and BW25113 *ΔlacY* LacY$^{mEos\text{-}Pop}$ cells (Figure 4e). Both strains show some membrane deformations indicative of plasmolysis, and the effects are more pronounced with the 3-fold than with the 2-fold osmolarity increase. However, we find fewer deformed BW25113 *ΔlacY* LacY$^{mEos\text{-}Pop}$ cells than BW25113 *ΔlacY* LacY^{mEos}; 24±7 % versus 53±8 % at the 3-fold osmolarity increase (number of analyzed fields of view is 5, two-sided t-test p-value = 0.0003). We find almost no deformed BW25113 *ΔlacY* LacY$^{mEos\text{-}Pop}$ cells at 2-fold osmolarity increase, which suggests that membrane-bound biomolecular condensates support the cytoplasmic membrane and reduce its deformation under hyperosmotic stress. A smaller degree of plasmolysis will diminish the volume decrease, and this may explain the higher U_{MAX} of LacY$^{mEos\text{-}Pop}$ expressing cells.

PopTag is driving the co-condensation of LacY and LacZ *in vivo*

Heterocondensation of cytoplasmic and membrane proteins has to the best of our knowledge not been explored but could potentially speed up reaction networks by direct pass on of substrates from transporter to enzyme. Hence, we co-expressed LacY and LacZ fusions with mEos3.2 and mRuby fluorescent proteins, respectively, with and without C-terminal PopTag (Table 1). We visualized the localization of membrane (LacY) and cytoplasmic (LacZ) protein for all combinations with and without PopTag by confocal laser-scanning fluorescence microscopy (Figure 5a).

LacY^{mEos} distributed homogeneously across the membrane and LacY$^{mEos\text{-}Pop}$ was predominantly present at the cell poles with smaller clusters in the lateral membrane, independent of co-expression of either LacZ^{mRuby} or LacZ$^{mRuby\text{-}Pop}$. LacZ^{mRuby} distributed mostly homogeneously in the cytoplasm, independent of co-expression of LacY^{mEos} or LacY$^{mEos\text{-}Pop}$; some inclusion bodies are visible at the cell poles, which is expected as β-galactosidase fusions are prone to aggregation[30,31], even at low inducer concentration (0.000001% w/v L-rhamnose) and 30 °C in minimal media. Remarkably, LacZ$^{mRuby\text{-}Pop}$ is localized differently in cells producing LacY^{mEos} and LacY$^{mEos\text{-}Pop}$. In BW25113 LacY^{mEos}-LacZ$^{mRuby\text{-}Pop}$ cells, LacZ$^{mRuby\text{-}Pop}$ forms spherical condensates at the cell poles, while in BW25113 LacY$^{mEos\text{-}Pop}$-LacZ$^{mRuby\text{-}Pop}$ cells we observe two different morphologies (Figure 5a). In the first, more frequent, scenario, LacZ$^{mRuby\text{-}Pop}$ forms large dome-shaped condensates at the cell poles and smaller condensates in the lateral membrane

colocalizing with LacY$^{mEos\text{-}Pop}$. In the second, less frequent, scenario, LacZ$^{mRuby\text{-}Pop}$ forms spherical condensates at the cell poles without smaller condensates in the lateral membrane. We hypothesize that in scenario I LacZ$^{mRuby\text{-}Pop}$ fully covers the in-membrane condensate of LacY$^{mEos\text{-}Pop}$, and in scenario II, large cytosolic condensates of LacZ$^{mRuby\text{-}Pop}$ only partially interact with in-membrane condensates of LacY$^{mEos\text{-}Pop}$. Co-localization of LacY and LacZ in all measured conditions was quantified by Pearson correlation coefficient with Costes thresholding. A high positive correlation was observed for LacY$^{mEos\text{-}Pop}$-LacZ$^{mRuby\text{-}Pop}$ (r = 0.81) and no or negative correlation for other conditions: -0.12 for LacY^{mEos}-LacZ^{mRuby}, -0.02 for LacY^{mEos}-LacZ$^{mRuby\text{-}Pop}$ and -0.41 for LacY$^{mEos\text{-}Pop}$-LacZ^{mRuby}.

FRAP measurements of the polar LacY$^{mEos\text{-}Pop}$ condensates, co-expressed with LacZ$^{mRuby\text{-}Pop}$, showed similar recovery patterns as observed with LacY$^{mEos\text{-}Pop}$ alone (Supplementary Figure 9). The half-time of recovery was 134 ± 47 sec for LacY$^{mEos\text{-}Pop}$ alone and 103 ± 19 seconds for LacY$^{mEos\text{-}Pop}$ in heterocondensates (the extra sum-of-squares F test p-value = 0.71), and the extents of recovery were 0.1409 ± 0.009 for LacY$^{mEos\text{-}Pop}$ alone and 0.128 ± 0.009 for LacY$^{mEos\text{-}Pop}$ in heterocondensates (extra sum-of-squares F test p-value = 0.35). These data indicate that LacY$^{mEos\text{-}Pop}$ condensates have similar materials properties when expressed alone or with LacZ$^{mRuby\text{-}Pop}$.

Transmission electron microscopy of BW25113 LacY$^{mEos\text{-}Pop}$-LacZ$^{mRuby\text{-}Pop\text{-}}$ also shows two scenarios of heterocondensate formation (Figure 5b, Supplementary Figure 10). Scenario I was observed in 5 out of 15 cell sections and shows the electron-dense region at the cytoplasmic face of the inner membrane, and it is thicker (~50 nm) than that of BW25113 LacY$^{mEos\text{-}Pop}$ cells (~10 nm, Figure 5b, left). Interestingly, in one cell, a large electron-dense region is seen in the cytoplasm, which is partially in contact with a thin (~10 nm) electron-dense region on the inner membrane (Figure 5b, right); this may represent scenario II of the confocal images (Figure 5a). These two scenarios correlate with two types of LacZ$^{mRuby\text{-}Pop}$ condensates, dome-shaped (more frequent) and spherical (less frequent) that are observed by confocal laser-scanning microscopy at the cell poles of BW25113 LacY$^{mEos\text{-}Pop}$-LacZ$^{mRuby\text{-}Pop}$ cells (Figure 5a). The two scenarios can be rationalized when LacY and LacZ have different expression levels: Scenario I would occur when the levels are similar, and Scenario II if LacZ is expressed at a higher level than LacY. We conclude that LacY^{Pop} and LacZ^{Pop} form heterocondensates of varying architectures that are anchored to the inner membrane of *E. coli*.

We then assessed the activity of LacY and LacZ in the heterocondensates. We constructed *E. coli* strains without mEos3.2 and mRuby to enable fluorescent read-out of LacZ activity with 4-methylumbelliferyl β-D-galactopyranoside as substrate[32,33]. The strains are named BW25113 *ΔlacY* LacY-LacZ, BW25113 *ΔlacY* LacY^{Pop}-LacZ, BW25113 *ΔlacY* LacY-LacZ^{Pop} and BW25113 *ΔlacY* LacY^{Pop}-LacZ^{Pop} (for details see Table 1). LacY activity was similar across all these strains as evaluated by ^{14}C-lactose uptake measurements (Supplementary Figure 11). The fluorescent substrate, 4-methylumbelliferyl β-D-galactopyranoside (β-MUG), is transported by LacY[33] and

hydrolyzed by LacZ. The transport negative strain, BW25113 *ΔlacY*, shows a slight decrease in signal over time, which does not reflect β-galactosidase activity. Strains expressing LacY and LacZ, with or without PopTag, hydrolyze β-MUG, and we estimated the β-galactosidase activity from the slope of the linear increase of fluorescent signal over time (Supplementary Figure 12). The fluorescence data were adjusted for the amounts of expressed β-galactosidase, determined by fluorescence imaging of SDS-PAGE separated *E. coli* lysates of LacZ-mRuby fusions, to obtain the specific β-galactosidase activity (Supplementary Figure 13). The activities of LacZ in all strains were normalized to the mean activity in BW25113 *ΔlacY* LacY-LacZ cells, which was 1.00±0.03 a.u. The activity increases to 1.62±0.05 a.u. in BW25113 *ΔlacY* LacY-LacZ^{Pop} cells, but decreases to 0.80±0.02 a.u. and 0.82±0.04 a.u. in BW25113 *ΔlacY* LacY^{Pop}-LacZ and BW25113 *ΔlacY* LacY^{Pop}-LacZ^{Pop} cells, respectively (Figure 5c). Clearly, the activity of β-galactosidase is highest when the protein is present in homocondensate and somewhat reduced in heterocondensates with LacY.

Discussion

Coacervate-membrane interactions and membrane-anchored biomolecular condensates have been observed[16], but mechanistic insight into their cellular organization and function is lacking, and membrane-anchored cellular heterocondensates have not been studied at all. We now provide a systematic study in this direction, using lactose metabolism in *Escherichia coli* as test case and a small (7 KDa) condensation tag, derived from the PopZ protein from *Caulobacter vibrioides*, to induce condensation. Figure 2c shows that the PopTag has three amphipathic α-helices with a high hydrophobic moment, and the hydrophobic faces of two of the helices (H1 and H2) form the main "stickers" for condensation as shown by our MD simulations. The PopTag provides an orthogonal, non-native tool to study liquid-liquid phase separation both *in vitro* and *in vivo*.

Using fluorescence microscopy, we show that LacY$^{mEos\text{-}Pop}$ forms larger biomolecular condensates at the cell poles and smaller ones in the lateral membrane of *E. coli* (Figure 1a,b). Molecular dynamics simulations confirm that the condensate formation is driven by hydrophobic interactions between PopTag's amphipathic α-helices. Using electron microscopy, we confirm that LacY$^{mEos\text{-}Pop}$ condensates localize on the cytoplasmic face of the inner membrane without disturbing membrane shape and integrity (Figure 1h). From the ^{14}C-lactose uptake assays, we see that LacY$^{mEos\text{-}Pop}$ is functional within condensates (Figure 4a). In FRAP experiments with LacY$^{mEos\text{-}Pop}$, we observe only partial (~14%) fluorescence recovery at the bleached cell pole without major decrease in fluorescence at the opposite pole, indicating that on the observed time scales the protein mostly redistributes between the pole and the lateral membrane, but not between two poles (Figure 1d, Supplementary Figure 1). We argue that the number of multivalent interactions between the PopTags is on average lower in the small lateral membrane condensates than in the

pole condensates, enabling LacY$^{mEos\text{-}Pop}$ to escape more easily than from the larger pole condensates (smaller perimeter/surface area ratio). This is also supported by the lack of fluorescence recovery after bleaching of the LacY$^{mEos\text{-}Pop}$ condensates on the lateral membrane. A partial fluorescence recovery has also been observed for cytoplasmic mCherry-PopTag fusion[18]. Unlike cytoplasmic mCherry-PopTag, LacY$^{mEos\text{-}Pop}$ forms multiple small condensates in the lateral membrane alongside with two major polar condensates. A localization pattern akin that of LacY$^{mEos\text{-}Pop}$ has been observed for the natively phase-separated membrane protein Rv1747 in *M. tuberculosis*[8], but the functional implications of the heterogenous membrane localization have not been studied.

Our experiments with cell shape and nucleoid content perturbations shed light on the mechanism governing the predominant pole localization of LacY$^{mEos\text{-}Pop}$ condensates. Using cells harboring multiple nucleoids and cells with degraded nucleoid, we show that nucleoid exclusion is not the driving force for formation of LacY$^{mEos\text{-}Pop}$ condensates at the poles (Figure 2a,b,c). Instead, the membrane geometry and most likely curvature is important for pole localization of the membrane condensates: the LacY$^{mEos\text{-}Pop}$ condensates redistribute in the membrane upon spheroplast formation, and localize to the high-curvature regions in osmotically upshifted spheroplasts (Figure 3d,e, Supplementary Video 2).

We hypothesize that local changes in the surface-to-volume ratio of the pre-membrane condensate plays a role in the curvature-driven polar localization of LacY$^{mEos\text{-}Pop}$. We consider a model, where PopTag drives the condensation of LacY$^{mEos\text{-}Pop}$ within a pre-membrane volume of thickness *d*, which is determined by the length of PopTag and the linker (connected to the last transmembrane segment of LacY). For the same area of membrane surface covered by LacY, a smaller pre-membrane volume is accessible for PopTag if the membrane is curved, leading to a higher local concentration that is critical for condensation (Figure 6b). An increase in concentration enhances phase-separation of LacY$^{mEos\text{-}Pop}$ at the areas of the higher curvature. For the 10-nm thick pre-membrane volume, the expected local increase of the concentration at the cell pole with radius of about 300 nm is only 3%. Although this change in concentration is most likely insufficient to be a sole reason for the observed polar localization of LacY$^{mEos\text{-}Pop}$, we speculate that it can act synergistically with other mechanisms governing the distribution of membrane protein-based condensates. Alternative mechanisms that could affect polar localization of LacY$^{mEos\text{-}Pop}$ condensates include: (1) specific interactions with biomolecules (e.g. cardiolipin[34,35]) partitioning at the cell poles, (2) physical trapping of condensates by large membrane protein assemblies at the cell poles (similar to trapping of chemoreceptors by Tol-Pal complexes[36]), and (3) progressive displacement of the cell wall components toward the poles upon cell elongation (similar to displacement of ActA in *Listeria monocytogenes*[37,38]). However, these mechanisms are likely disrupted when cells are spheroplasted and subsequently plasmolysed. Yet, LacY$^{mEos\text{-}Pop}$ localizes to the highly curved concave regions of the cytoplasmic membrane upon osmotic upshift. Under conditions of hyperosmotic stress, the ionic strength,

pH and macromolecular crowding of the cell change, but we have no evidence that these parameters play direct roles in the localization of LacY$^{mEos\text{-}Pop}$. We identify local membrane curvature as the main factor for the redistribution of LacY$^{mEos\text{-}Pop}$, because condensate formation is already observed at the cell poles in non-stressed *E. coli*.

Cells with LacY$^{mEos\text{-}Pop}$ accumulate lactose to higher final concentrations (Figure 4b), suggesting either a bigger cell volume, or higher import activity of LacY$^{mEos\text{-}Pop}$ compared to LacY^{mEos}, assuming that the driving force for lactose-proton symport is the same. The transport of lactose and proton proceeds via the formation of a ternary complex with the LacY protein, but the coupling (ternary lactose-H^+-LacY complex) is not always strict, which can lead to different accumulation levels at the same driving force[39,40]. The coupling efficiency of secondary active transporters like LacY can be altered by mutations or a different membrane environment. It is thus possible that the higher accumulation by LacY$^{mEos\text{-}Pop}$ reflects a higher coupling efficiency due to altered by protein-protein interactions within the condensate or and by the distinct protein and lipid environment of the cell pole.

The PopTag scaffold could also mechanically support the membrane, explaining the lesser deformations in LacY$^{mEos\text{-}Pop}$ cells under hyperosmotic stress (Figure 4e). The PopTag scaffold may also affect other biophysical properties of the membrane, e.g. viscosity, as was previously shown *in vitro* for other membrane-associated biomolecular condensates[16,41]. However, the important conclusion that we draw is that the condensation of LacY does not negatively affect its activity and may even increase the performance of the protein.

Using PopTag, we created a heterocondensate of a cytoplasmic enzyme and a membrane transport protein, LacZ and LacY, *in vivo.* The maximal uptake rates in all LacY and LacZ combinations are similar (Supplementary Figure 11), while β-galactosidase activity is different. The β-galactosidase activity of LacZ^{Pop} is ~1.6 times higher than that of LacZ, which is in line with the increase of LacZ activity in peptide-peptide condensates *in vitro*, also using β-MUG as substrate[32]. The increased activity of LacZ in condensates, both *in vivo* and *in vitro*, could be due to the stabilization of tetrameric LacZ, because the condensate microenvironment with higher local LacZ concentration might shift the oligomeric equilibrium towards active tetramers[42]. When LacY and LacZ form a heterocondensate, the β-galactosidase activity is decreased compared to the condensed LacZ alone. We attribute the decrease in activity to the dimensionality of the LacZ condensates, and β-galactosidase having a higher activity in 3D condensates (LacY-LacZ^{Pop}) than in 2D (scenario I in Figure 5b) or 2.5D (scenario II in Figure 5b). LacZ homocondensates may have the more optimal crowding and surface-to-volume ratio to stabilize the enzyme or possibly the influx of substrate.

If LacZ$^{mRuby\text{-}Pop}$ protein is added to the model of curvature-dependent polar localization of LacY$^{mEos\text{-}Pop}$ (Figure 6b,c), the thickness of the pre-membrane volume increases to ~50 nm, resulting in a more pronounced, up to 20%, local increase of the concentration. This makes the

formation of heterocondensates at the poles more favorable than the assembly of homotypic $LacY^{mEos\text{-}Pop}$ condensates.

In conclusion, we show that $LacY^{Pop}$ forms biomolecular condensates that localize at the cell poles of *E. coli* in a curvature-dependent manner; under some conditions the condensed protein ($LacY^{Pop}$) outperforms wild-type LacY in transport activity and can form functional heterocondensates with its metabolic partner $LacZ^{Pop}$. Having characterized the structure and interactions of $LacY^{Pop}$ membrane condensates experimentally and computationally, engineering specialized condensation tags with alternative interaction modes may further optimize the coupling between membrane transporters and metabolic networks. We propose that the variety of natively-disordered regions in a wide range of integral membrane proteins warrant further investigation[8,43–45]. They may not solely be regulatory sites that tune protein activity via post-translational modifications but also play a role in the supramolecular organization of membrane-bound complexes. Our research provides a framework to engineer cells and exploit the co-localization of molecules in metabolic networks, stabilize proteins in biomolecular condensates, and/or tune enzymatic efficiency and protein localization *in vivo*. Collectively, our findings contribute to the emerging field of liquid-liquid phase separation and the engineering of spatially-controlled metabolic reactions networks and their coupling to membrane-bound processes.

Methods

Strains and plasmids

E. coli strain BW25113 [F-, *Δ(araD-araB)567*, *ΔlacZ4787*(::rrnB-3), *λ-*, *rph-1*, *Δ(rhaD-rhaB)568*, *hsdR514*] was used for most experiments. For storage and cloning we used *E. coli* DH5α [[F-, *Δ(argF-lac)169*, *φ80dlacZ58(M15)*, *ΔphoA8*, *glnX44(AS)*, *λ-*, *deoR481*, *rfbC1*, *gyrA96(NalR)*, *recA1, endA1, thiE1, hsdR17*]. All strains and plasmids used are found in Table 1. Plasmids were constructed with the USER cloning protocol and transformed to *E. coli* via the heat-shock method and subsequently checked via Sanger sequencing by Eurofins Genomics. Plasmid DNA was isolated with the NucleoSpin Plasmid kit (MACHEREYNAGEL). All protein sequences and primers used in this study are shown in Supplementary Tables 1 and 2 respectively.

Culturing conditions

Antibiotic concentrations used as a selective marker were 100 µg/ml ampicillin (dissolved as 1000x stock) in 50% EtOH, 20 µg/ml chloramphenicol (dissolved as 1000x stock) and 10 µg/ml tetracycline (dissolved as 1000x stock). Lysogeny broth (LB) was prepared using standard recipe and sterilized by autoclaving. Mops-buffered minimal media (MBM) was prepared as described in[21,46]. All measurements were performed in the MBM media after overnight preculturing in LB followed by overnight preculturing in MBM media as described in[21,22]. Briefly 3 mL of LB media

supplemented with antibiotic(s), if strains harbor plasmids, was inoculated with a single colony of *E. coli* and grown overnight at 30°C with shaking at 180 rpm, after which the preculture in LB was diluted 100-fold in MBM supplemented with 0.1% (v/v) glycerol plus antibiotic(s) and incubated overnight at 30°C with shaking at 180 rpm. On the next day, the MBM preculture was diluted into fresh, prewarmed MBM with 0.1% (v/v) glycerol plus antibiotic(s) to a final OD_{600} of 0.05 and grown for the needed amount of time, typically 4 h until an OD_{600} of 0.15 was reached. Unless stated otherwise, expression of *lacY* fusion genes from pBAD was induced by 0.1% L-arabinose for 4 hours, expression of *lacZ* fusion genes from pACYC was induced by 0.000001% L-rhamnose for 4 hours.

For all microscopy measurements cells were grown in 3 mL of MBM media for 4 hours. 1 mL of cell culture was spun down and resuspended in 100 µL of remaining media. 2 µL of cell culture were put on cleaned (by sonication in 5M KOH) 1.5H high-precision glass slides (170 µm thickness, Carl Roth GmbH & Co KG) and immobilized by agarose pads as described elsewhere[21,22].

For electron microscopy, lactose transport and β-galactosidase activity assays, cells were grown using the following protocol: 3 mL of LB preculture (with the appropriate antibiotic(s)) was inoculated with a single colony of the appropriate *E. coli* strain and grown overnight at 30 °C with shaking at 180 rpm. The next day, the LB preculture was diluted 100x into 20 mL of MBM minimal media supplemented with 0.1% glycerol plus antibiotic(s) and grown overnight at 30 °C with shaking at 180 rpm. The next day, the MBM preculture was diluted into 100 mL of MBM media with 0.1% glycerol plus antibiotic(s) to reach a final OD_{600} of 0.05. Induction of genes coding for LacY and LacZ variants was done by adding 500 µL of 20% arabinose (f.c. 0.1%) and 100 µL of 0.001% rhamnose (f.c. 0.000001%), respectively, and the cells were incubated for 4 hours to reach an OD_{600} of ~0.15.

To block the division of *E. coli* 20 µg/ml of cephalexin dissolved in MQ water was added to the cells at the moment of dilution to OD_{600} of 0.05 and treatment was continued for 4 or 7 hours.

For nucleoid degradation *E. coli* LY177 [*ΔrecA-Tc ydeO::I-Sce1*^{CS}*, ilvA::I-Sce1*^{CS}] was used[25]. Expression of the *I-SceI* gene was induced with 0.2% L-Arabinose for 2 hours from pSN1 and *lacY* fusions were expressed from pACYC vector and 0.5% L-Rhamnose as inducer. In the liquid media and agarose plates for *E. coli* LY177, carrying pACYC, 0.2% glucose was used to reduce the leaky expression of the gene coding for *I-SceI* endonuclease (J. Losa, personal communication, 2024). To obtain the *E. coli* LY177 with two plasmids, the cells were first transformed with the pACYC vector, carrying genes of the *lacY* variants, and plated on agar with chloramphenicol plus tetracycline. Next, a new batch of competent cells was made from these cells, grown in the presence of chloramphenicol plus tetracycline. They were subsequently transformed with pSN1, carrying endonuclease the *I-SceI* gene, and plated on agar with chloramphenicol, tetracycline,

ampicillin supplemented with 0.2% glucose. The cells were used within a week to prevent nucleoid degradation due to leaky expression of *I-SceI*.

The protocol for spheroplasts preparation was adapted from[26,27]. Cells were grown in the presence of 20 µg/ml cephalexin for 4 hours, while the gene of interest was expressed. Then 1 ml of cell culture was concentrated two times by centrifugation at 8,200 g in a Spectrafuge™ 16M centrifuge for 1 min. To 500 µL of cell culture 500 µL of 2M glucose solution, 5 µL of 200 µg/mL lysozyme plus 5 µL of 0.5 M EDTA (pH 8.0) were added, and the cells were incubated at room temperature for 15 min. 2.5 µL of 1 M $MgCl_2$ was added to quench the spheroplasting and cells were concentrated to 100 µL.

Wide-field fluorescence microscopy

A Zeiss Axio Observer microscope with 100x oil immersion objective (1.4 NA) was used for imaging of *E. coli* cells. Fluorescence of mEos3.2 green state was excited by 470 nm LED and the emission was collected in the 500-550 nm wavelength range. For nucleoid staining we used DAPI at a final concentration of 15µM (incubated for 15 min), and the fluorescence was excited by 365 nm LED and the emitted light was collected in the 420-470 nm range. Phase contrast for intact bacterial cell or brightfield images for spheroplasts were also collected.

Fluorescence recovery after photobleaching (FRAP)

For non-condensated $LacY^{mEos}$, FRAP measurements were performed on Zeiss LSM 710 ConfoCor 3 equipped with a Plan-Apochromat 100x oil-immersion objective (NA=1.40). The 488-nm laser was used for fluorescence recording at 15% laser intensity. Individual cells were measured in fields of view of 8.94 x 8.94 µm2 (512 x 512 pixels), roughly half of a cell was used as a bleached region of interest (ROI). Measurements were performed at maximal scanning speed, with pixel dwell time of 0.39 µs. Prior to bleaching, 5 fluorescence images were taken every 0.243 s. During bleaching, the ROI was scanned once with 488-nm illumination at 100% laser intensity. After bleaching, 15 fluorescence images were taken every 0.243 s. In total, n=21 BW25113 $LacY^{mEos}$ cells were measured. Because the intensity of the readout laser also bleaches $LacY^{mEos}$ and the mobility of the protein is relatively high, we also measured fluorescent signal over time from the non-bleached half of a cell and used it to correct the recovery for bleaching during readout.

For condensed $LacY^{mEos\text{-}Pop}$, FRAP measurements were performed on Leica Stellaris 8 microscope equipped with 63x Plan-Apochromat water-immersion objective (NA 1.20). For fluorescence recording, a 488-nm laser was used at 10% intensity, depending on the brightness of the cells. Several cells were measured simultaneously in the same field of view of 64.87 x 64.87 µm (512 x 512 pixels), with one bleached region of interest (ROI) per cell. ROIs were defined

individually for each cell based on its geometry: polar regions (n=20) enclose the polar condensate, lateral membrane regions (n=25) cover the membrane area between the two polar condensates, and whole-cell ROIs (n=23) include the entire cell (Supplementary Figure 2). Measurements were performed at maximal scanning speed, with pixel dwell time of 1.76 µs. Prior to bleaching, 5 fluorescence images were taken every 1 s. During bleaching, the ROIs were scanned 30 times with 488-nm illumination at 100% laser intensity. After bleaching, fluorescence images were taken every 1 min for a total of 20 min. Contrast-based autofocus with a 20 µm range was applied before every measurement to prevent z-drift over a long timescale. Additionally, to test whether fluorescence recovery at the cell poles was due to newly synthesized protein, BW25113 LacY$^{mEos\text{-}Pop}$ cells were treated with 20 µg/mL chloramphenicol for one hour (after 4h of protein expression), prior to the FRAP measurements (n=17 cells).

Recovery data for both LacY^{mEos} and LacY$^{mEos\text{-}Pop}$ were normalized by setting the average fluorescence intensity before the photobleaching step to 1 and the intensity immediately after the photobleaching step to 0. The recovery curve w.as fitted with the exponential plateau equation.

Single-molecule displacement mapping (SMdM)

SMdM measurements were performed as described previously[21,22] with some modifications. Briefly, a 405 nm laser pulse (OBIS 405 LX, 50 mW max. power) was used to photoconvert mEos3.2 from a green fluorescent state (507 nm ex. / 516 nm em.) to red (572 nm ex. / 580 nm em.), and two readout beams of 561 nm laser (OBIS LS 561-150) were used with time separation (Δt) of 10 ms. Time separation between the excitation 561 nm pulses was increased from 1.5 ms to 10 ms as mobility of slow diffusing proteins is better captured at higher Δt values[23]. The emitted signal was collected by an EM-CCD camera (C9100-13, Hamamatsu), using an ET 605/70 M bypass filter (Chroma).

ThunderSTORM plugin of ImageJ (https://zitmen.github.io/thunderstorm/) was used for the peak detection to obtain single-protein localizations along with the localization uncertainty values. We used localization uncertainty values for the correction of the measured diffusion coefficient. Knowing the localization uncertainty, we can estimate the apparent diffusion coefficient, which is related to this uncertainty ($D_{loc.unc}$), using the following equation:

$$\sqrt{\sigma_{start}^2 + \sigma_{end}^2} = \sqrt{2nD_{loc.unc}\Delta t} \quad (1)$$

Where *n* is number of dimensions, σ_{start} and σ_{end} are uncertainties in localization of starting and ending positions of the protein displacements over the Δt time period. Assuming

that the localization uncertainties for the start and end positions are equal and that n = 2, equation 1 simplifies to:

$$D_{loc.unc} = \frac{\sigma_{mean}^2}{2\Delta t} \quad (2)$$

To obtain the diffusion coefficient of moving proteins, the probability density distribution of measured displacements as a function of time separation (Δt) was fitted with an adjusted probability density function (PDF) of a 2-dimensional random-walk diffusion model with background correction and normalized for the maximum search radius[47]:

$$p(r,\Delta\mathrm{t}) = \frac{1}{1-e^{-\frac{r_{max}^2}{4D_L\Delta t}+\frac{b}{2}r_2^{max}}}\left(\frac{2r}{4D_L\Delta\mathrm{t}}e^{-\frac{r^2}{4D_L\Delta\mathrm{t}}}+br\right) \quad (3)$$

Where D_L is the lateral diffusion coefficient, r is the peak-to-peak displacement, Δt is the time separation between 561 nm readout laser pulses (10 ms in this case), b is a background correction coefficient, and r_{max} is 200 nm. Because proteins with lower mobility are more affected by localization uncertainty, we subtract the $D_{loc.unc}$ from the D_L to correct for this effect.

To reconstruct diffusion maps we binned each cell into square selections with a side of 100 nm and fitted the displacements starting within a bin with equation 3. This was done for bins with at least 100 displacements.

Photoactivated localization microscopy (PALM)

For super-resolution microscopy, the same home-built setup was used as for SMdM measurements. To convert and excite mEos3.2 fluorescent protein we utilized the same pulse pattern as for SMdM measurements. Briefly, a low-intensity 1 ms 405 nm photoactivation pulse was followed by a 0.5 ms 561 nm readout pulse within the same camera frame and again in the subsequent frame; frame time of the camera was 17.86 ms for 25 x 25 μm^2. This sequence was repeated for 100,000 frames. Peak detection was done using ThunderSTORM plugin [https://zitmen.github.io/thunderstorm/] for ImageJ software, using appropriate camera parameters. Super resolution images were reconstructed using a custom Python script[48]. The localized molecules, resulting in the form of sub-pixel x,y coordinates along with their lateral localization uncertainties, were subsequently plotted in reconstruction images as 2D Gaussians centered at (x,y) with σ equal to the corresponding localization uncertainty.

Confocal microscopy

The Leica Stellaris 8 microscope with white light laser was used to localize different variants of LacY-mEos3.2 and LacZ-mRuby in *E. coli* cells. For excitation of mEos3.2, 489 nm laser

light was used and the emitted light in the 500-581 nm range was collected; 560 nm laser was used to excite mRuby and emitted light in the range 581-700 nm was collected.

Electron microscopy

Cells were grown as described in "Culturing conditions" section. *E. coli* cells were concentrated by centrifugation at 4,000 x *g* to the minimal volume possible (paste-like suspension) and transferred to a 3 mm copper gold-plated type B (flat-surfaced) carrier (Leica). Cells immobilized by high pressure freezing (EM ICE, Leica) were freeze-substituted in 1% (w/v) OsO_4 plus 0.5% uranyl acetate in acetone with 5% water, using the quick freeze substitution method[49]. Samples were embedded in Epon resin and ultra-thin sections of approximately 100 nm were collected on formvar-coated and carbon evaporated copper grids and inspected using a TALOS L120C (Thermo Scientific) transmission electron microscope (TEM). For the ultrastructural analysis, we have visually selected cells where the inner and outer membranes are clearly visible and a periplasm thickened at the cell pole; we excluded cells that were sectioned at high angles relative to the long axis of the cell. This analysis was blinded to the experiment group and independently performed by two researchers (DL and IM), and only cells labeled as condensate positive by both researchers were marked as "positive" in the final analysis. Thickness of the pre-membrane electron-dense layer was analyzed by line profiles of the electron density perpendicular to the membrane, using ImageJ software.

Molecular dynamics simulations

Protein structures (LacY, LacY^{Pop}, and PopTag) were modelled using AlphaFold3[50]. All simulations were performed using Gromacs 2024.3 with the Martini 3 force field[51–53].

Topologies and initial conformations for all protein structures were generated from their all-atom counterparts using Martinize2 (Supplementary Table 3)[54]. The coarse-grained Martini 3 force field was chosen over all-atom representations to enable longer timescale simulations while maintaining sufficient chemical detail for protein-protein interactions and membrane dynamics. The Martini3 protein model requires explicit assignment of secondary structure elements during model building. Since opening of the periplasmic cavity is the rate-limiting transport step in LacY, we applied structural restraints derived from the outward-facing structure (PDB:6VBG[55]) to the AlphaFold3 models, which overwise predicts the inward-facing state most abundant in the PDB[56].

For the PopTag, we assigned these structural elements based on the Jpred tool and all-atom simulations from a previous study, since AlphaFold predictions struggle to represent the ensemble characteristics of intrinsically disordered regions[17,56,57]. The three helices motifs of the PopTag were modelled as H1 (residues $14-31$), H2 (residues $40-58$), and H3 (residues $62-76$), with remaining residues modelled as coils. For the intrinsically disordered region at the N-

terminus of PopTag (residues $1-13$), Martini parameters were tuned using the -idr-tune flag in Martinize2, to better reproduce the expanded conformations of disordered regions[59].

Placing the proteins into the simulation box was done using Bentopy, while the membranes were constructed using the *insane* tool[60,61]. Lipid compositions were chosen to represent the *E. coli* inner membrane (75% POPE, 20% POPG, 5% cardiolipin)[62]. During system preparation, each simulation box was solvated, neutralized, and NaCl was added to reach a concentration of 150 mM.

The slab condensate model was constructed with 100 molecules contained within the central 15 nm of a $15 \times 15 \times 50$ nm simulation box resulting in a concentration of 15mM of protein. For the membrane simulations, 9 copies of LacY or LacY^{Pop} were placed in a regular grid configuration into a membrane of 35nm x 35nm maintaining equal distances between adjacent membrane proteins.

The initial configurations underwent energy minimization using Gromacs' steepest descent algorithm, followed by equilibration and production simulations. Equilibration was conducted for 50 ns using a $10\ fs$ timestep, while production runs used a $20\ fs$ timestep for simulation time of 50 µs. The simulation convergence was verified by looking at the number of protein clusters over time, which converged during the simulation (see Supplementary Figure 4). Temperature and pressure were regulated during equilibration and production simulations using the v-rescale thermostat and c-rescale barostat respectively. All simulations employed semi-isotropic pressure coupling. For membrane simulations, pressure was maintained at $1\ bar$ ($\tau_p = 12\ ps$, $\beta = 3e^{-4}\ bar^{-1}$). For slab condensate simulations, pressure coupling in the xy-plane was disabled to maintain a fixed interface area, while a default pressure coupling along the z-axis was applied to allow the condensate to equilibrate to its natural density. All simulations were conducted at $300\ K$ ($\tau_t = 1\ ps$) with separate coupling groups for solvent, lipid, and protein when applicable.

Other nonbonded simulation parameters followed Martini3 recommendations for Gromacs, with specific settings for large membranes ($\text{verlet} - \text{buffer} - \text{tolerance} = -1, \text{rlist} = 1.35$ nm)[53,63,64]. All simulations were performed in triplicate for better statistics on the results. Analysis of the simulation data was performed using the MDAnalysis 2.9.0 Python library[65,66]. The protein-protein contacts were identified using a distance-based criterion, with residues considered in contact when their backbone beads are within 15 Å of each other. Backbone bead contacts were used for computational efficiency and validated against whole residue-residue contacts, confirming consistent results (Supplementary Figure 5a). The number of protein clusters was defined as the number of distinct protein groups where proteins within each group shared at least one residue-residue contact with another protein in that group. Within these clusters, the number of protein-protein contacts was quantified as the count of unique protein pairs in contact. Contact lifetime analysis revealed contacts persist for microsecond timescale, demonstrating stable protein associations beyond thermal fluctuations.

(Supplementary Figure 5b). For clarity, the time evolution traces of the protein cluster metrics were calculated over the whole production simulation and smoothed with a median filter with a window size of 25 ns. To create the contact maps, we calculated the specific residue-residue contacts across all simulation frames and determined their frequency. Snapshots of the molecular dynamics trajectories were rendered using Visual Molecular Dynamics (VMD 1.9.4a57) software[67] and figures were made using Matplotlib 3.9.2[68].

Transport assays

Cells were grown as described in "Culturing conditions" section. Part of the cells were taken for imaging and the rest was used for transport assays. After harvesting by centrifugation (10 min at 4,000 x *g*), the cells were resuspended to an OD_{600} of ~25 in MBM media plus 10 mM glucose, which was also used as assay buffer. [D-glucose-1-^{14}C] lactose (56 mCi/mmol) was purchased from American Radiolabeled Chemicals. For the assay concentrated cells were diluted into MBM media plus 10 mM glucose to an OD_{600} of 1 and prewarmed at 30°C. At time zero of the assay ^{14}C-lactose was added to a final concentration of 10 µM. The assay volume was 150 µL and at given time intervals (10, 40, 70, 100 and 150 sec), samples of 25 µL were taken and the transport reaction was quenched with 2 mL ice-cold 0.1 M LiCl, and the mixture was filtered immediately over prewetted nitrocellulose filters with a pore diameter of 0.45 µm (Protean, Cytiva). Subsequently, the filters were washed with 2 mL ice-cold 0.1 M LiCl and then dissolved in 2 mL Ultimagold TM scintillation fluid (Perkin Elmer). Radioactivity, reflecting the uptake of ^{14}C-lactose, was determined with a Perkin Elmer Tri-carb 2800TR scintillation counter.

For uptake of lactose under osmotic stress conditions, 12 µL of the MBM media in the assay and the quench buffer was replaced by 2 or 4 M NaCl to reach final additional concentration of 160 mM and 320 mM respectively.

β-Galactosidase activity assay

Cells were grown as described in "Culturing conditions" section. Cells are harvested by centrifugation at 4,000 x *g* at 4 °C for 10 min and concentrated to a final OD_{600} of 5 in phosphate-buffered saline (PBS, 0.40 g NaCl, 0.01 g KCl, 0.07 g Na_2HPO_4, 0.01 g KH_2PO_4 in 50 mL MQ water, pH 7.4) on ice. 190 µL of cells were added to a black µClear Flat Bottom 96-well plate for fluorescence measurements (Greiner). 10 µL of 1mM 4-methylumbelliferyl β-D-galactopyranoside (β-MUG) was added to each well, to reach a final concentration of 50 µM. Upon cleavage by β-galactosidase the emission maximum of β-MUG shifts from 375 to 445 nm; the increase at 445 nm was used to determine the β-galactosidase activity. The Spark Multimode plate reader (TECAN) was used to monitor the progress of the reaction at 445 nm at 30 °C with β-MUG excitation at 320 nm wavelength. Emission spectra were measured in the range of 345 – 550 nm, immediately after β-MUG addition and after the time-series measurement

(Supplementary Figure 14). Fluorescence at 445 nm wavelength was measured every minute for 19 minutes.

Statistics and Reproducibility

Data in the text presented as mean ± SD unless otherwise specified. Normality of data distribution was tested by the Shapiro-Wilk test. Two-side Student t-test was used at the significance level of 5 percent to compare mean values of two datasets. Linear or exponential plateau functions were fitted to the datasets using relevant regression models, and parameters of these models such as slope or plateau level were used to determine parameters for e.g. ^{14}C-lactose uptake. The fitting parameters of lactose uptake experiments and FRAP recovery curves, including recovery half-time and extent, were compared using the extra sum-of-squares F-test at the significance level of 5%. GraphPad Prism 10 software was used to perform all statistical tests and to make plots.

Fluorescent microscopy measurements presented in Figures 1a and 5a were done twice with similar results. Fluorescent microscopy measurements presented in Figures 3a, 3b, 3c, 3d, 3e and 4e were done ones with similar results on different fields of view. Electron microscopy measurements presented in Figures 1h and 5b were done once.

Data Availability

Raw microscopy, single-molecule displacement mapping and β-Galactosidase activity assay data generated in this study are available at DataverseNL repository[71]: [https://doi.org/10.34894/X8GI6H]. The raw counts per minute from the transport assays are available in the Source data file. The simulation input files and trajectories are available on Zenodo[72]: [https://doi.org/10.5281/zenodo.17335657]. Unless otherwise stated, all data supporting the results of this study can be found in the article, supplementary, and source data files. Source data are provided with this paper.

Code Availability

Code for the analysis of the molecular dynamic simulations available on Zenodo: [https://doi.org/10.5281/zenodo.17335657]. The developed code for modulating laser pulses, using a PCI-6602 programmable card (National Instruments), for SMdM analysis and PALM reconstruction is available at [https://doi.org/10.5281/zenodo.5911836] and [https://doi.org/10.5281/zenodo.14334015] as links to the Github repository of Membrane Enzymology Laboratory: [https://github.com/MembraneEnzymology/]

References

1. Azaldegui, C. A., Vecchiarelli, A. G. & Biteen, J. S. The emergence of phase separation as an organizing principle in bacteria. *Biophysical Journal* **120**, 1123–1138 (2021).
2. Alberti, S. & Hyman, A. A. Biomolecular condensates at the nexus of cellular stress, protein aggregation disease and ageing. *Nat Rev Mol Cell Biol* **22**, 196–213 (2021).
3. Spannl, S., Tereshchenko, M., Mastromarco, G. J., Ihn, S. J. & Lee, H. O. Biomolecular condensates in neurodegeneration and cancer. *Traffic* **20**, 890–911 (2019).
4. Saini, B. & Mukherjee, T. K. Biomolecular Condensates Regulate Enzymatic Activity under a Crowded Milieu: Synchronization of Liquid–Liquid Phase Separation and Enzymatic Transformation. *J. Phys. Chem. B* **127**, 180–193 (2023).
5. Ginell, G. M. & Holehouse, A. S. An Introduction to the Stickers-and-Spacers Framework as Applied to Biomolecular Condensates. in *Phase-Separated Biomolecular Condensates* (eds. Zhou, H.-X., Spille, J.-H. & Banerjee, P. R.) vol. 2563 95–116 (Springer US, New York, NY, 2023).
6. Holehouse, A. S. & Alberti, S. Molecular determinants of condensate composition. *Molecular Cell* **85**, 290–308 (2025).
7. Su, X. *et al.* Phase separation of signaling molecules promotes T cell receptor signal transduction. *Science* **352**, 595–599 (2016).
8. Heinkel, F. *et al.* Phase separation and clustering of an ABC transporter in *Mycobacterium tuberculosis*. *Proc. Natl. Acad. Sci. U.S.A.* **116**, 16326–16331 (2019).
9. Tan, W. *et al.* Phase separation modulates the assembly and dynamics of a polarity-related scaffold-signaling hub. *Nat Commun* **13**, 7181 (2022).

10. Tusnády, G. E., Dobson, L. & Tompa, P. Disordered regions in transmembrane proteins. *Biochimica et Biophysica Acta (BBA) - Biomembranes* **1848**, 2839–2848 (2015).
11. Khandelwal, N. K. & Tomasiak, T. M. Structural basis for autoinhibition by the dephosphorylated regulatory domain of Ycf1. *Nat Commun* **15**, 2389 (2024).
12. Fiedorczuk, K. *et al.* The structures of protein kinase A in complex with CFTR: Mechanisms of phosphorylation and noncatalytic activation. *Proc. Natl. Acad. Sci. U.S.A.* **121**, e2409049121 (2024).
13. Ukleja, M. *et al.* Flotillin-mediated stabilization of unfolded proteins in bacterial membrane microdomains. *Nat Commun* **15**, 5583 (2024).
14. López, D. & Kolter, R. Functional microdomains in bacterial membranes. *Genes Dev.* **24**, 1893–1902 (2010).
15. Gohrbandt, M. *et al.* Low membrane fluidity triggers lipid phase separation and protein segregation in living bacteria. *The EMBO Journal* **41**, e109800 (2022).
16. Mangiarotti, A. & Dimova, R. Biomolecular Condensates in Contact with Membranes. *Annual Review of Biophysics* **53**, 319–341 (2024).
17. Lasker, K. *et al.* The material properties of a bacterial-derived biomolecular condensate tune biological function in natural and synthetic systems. *Nat Commun* **13**, 5643 (2022).
18. Hoang, Y. *et al.* An experimental framework to assess biomolecular condensates in bacteria. *Nat Commun* **15**, 3222 (2024).
19. Bürgi, J., Xue, B., Uversky, V. N. & Van Der Goot, F. G. Intrinsic Disorder in Transmembrane Proteins: Roles in Signaling and Topology Prediction. *PLoS ONE* **11**, e0158594 (2016).

20. Xiang, L., Chen, K., Yan, R., Li, W. & Xu, K. Single-molecule displacement mapping unveils nanoscale heterogeneities in intracellular diffusivity. *Nat Methods* **17**, 524–530 (2020).
21. Śmigiel, W. M. *et al.* Protein diffusion in *Escherichia coli* cytoplasm scales with the mass of the complexes and is location dependent. *Sci. Adv.* **8**, eabo5387 (2022).
22. Linnik, D., Maslov, I., Punter, C. M. & Poolman, B. Dynamic structure of E. coli cytoplasm: supramolecular complexes and cell aging impact spatial distribution and mobility of proteins. *Commun Biol* **7**, 508 (2024).
23. Yan, R., Chen, K. & Xu, K. Probing Nanoscale Diffusional Heterogeneities in Cellular Membranes through Multidimensional Single-Molecule and Super-Resolution Microscopy. *J. Am. Chem. Soc.* **142**, 18866–18873 (2020).
24. Bailey, M. W., Bisicchia, P., Warren, B. T., Sherratt, D. J. & Männik, J. Evidence for Divisome Localization Mechanisms Independent of the Min System and SlmA in Escherichia coli. *PLoS Genet* **10**, e1004504 (2014).
25. Stracy, M. *et al.* Transient non-specific DNA binding dominates the target search of bacterial DNA-binding proteins. *Molecular Cell* **81**, 1499-1514.e6 (2021).
26. Takamori, S., Cicuta, P., Takeuchi, S. & Di Michele, L. DNA-assisted selective electrofusion (DASE) of *Escherichia coli* and giant lipid vesicles. *Nanoscale* **14**, 14255–14267 (2022).
27. Sun, Y., Sun, T.-L. & Huang, H. W. Physical Properties of Escherichia coli Spheroplast Membranes. *Biophysical Journal* **107**, 2082–2090 (2014).
28. Roberts, E., Magis, A., Ortiz, J. O., Baumeister, W. & Luthey-Schulten, Z. Noise Contributions in an Inducible Genetic Switch: A Whole-Cell Simulation Study. *PLoS Comput Biol* **7**, e1002010 (2011).

29. Culham, D. E., Romantsov, T. & Wood, J. M. Roles of K^+ , H^+ , H_2 O, and ΔΨ in Solute Transport Mediated by Major Facilitator Superfamily Members ProP and LacY. *Biochemistry* **47**, 8176–8185 (2008).

30. Mika, J. T., Van Den Bogaart, G., Veenhoff, L., Krasnikov, V. & Poolman, B. Molecular sieving properties of the cytoplasm of *Escherichia coli* and consequences of osmotic stress. *Molecular Microbiology* **77**, 200–207 (2010).

31. Elowitz, M. B., Surette, M. G., Wolf, P.-E., Stock, J. B. & Leibler, S. Protein Mobility in the Cytoplasm of *Escherichia coli*. *J Bacteriol* **181**, 197–203 (1999).

32. Harris, R., Veretnik, S., Dewan, S., Baruch Leshem, A. & Lampel, A. Regulation of enzymatic reactions by chemical composition of peptide biomolecular condensates. *Commun Chem* **7**, 90 (2024).

33. Smirnova, I. *et al.* Oversized galactosides as a probe for conformational dynamics in LacY. *Proc. Natl. Acad. Sci. U.S.A.* **115**, 4146–4151 (2018).

34. Renner, L. D. & Weibel, D. B. Cardiolipin microdomains localize to negatively curved regions of *Escherichia coli* membranes. *Proc. Natl. Acad. Sci. U.S.A.* **108**, 6264–6269 (2011).

35. Romantsov, T. *et al.* Cardiolipin promotes polar localization of osmosensory transporter ProP in *Escherichia coli*: Cardiolipin and osmoregulation in *Escherichia coli*. *Molecular Microbiology* **64**, 1455–1465 (2007).

36. Santos, T. M. A., Lin, T., Rajendran, M., Anderson, S. M. & Weibel, D. B. Polar localization of *E scherichia coli* chemoreceptors requires an intact TOL – PAL complex. *Molecular Microbiology* **92**, 985–1004 (2014).

37. Rafelski, S. M. & Theriot, J. A. Mechanism of polarization of *Listeria monocytogenes* surface protein ActA. *Molecular Microbiology* **59**, 1262–1279 (2006).

38. De Pedro, M. A., Grünfelder, C. G. & Schwarz, H. Restricted Mobility of Cell Surface Proteins in the Polar Regions of *Escherichia coli*. *J Bacteriol* **186**, 2594–2602 (2004).

39. Lolkema, J. S. & Poolman, B. Uncoupling in Secondary Transport Proteins. *Journal of Biological Chemistry* **270**, 12670–12676 (1995).

40. Henderson, R. K., Fendler, K. & Poolman, B. Coupling efficiency of secondary active transporters. *Current Opinion in Biotechnology* **58**, 62–71 (2019).

41. Mangiarotti, A. *et al.* Biomolecular condensates modulate membrane lipid packing and hydration. *Nat Commun* **14**, 6081 (2023).

42. Juers, D. H., Matthews, B. W. & Huber, R. E. *LacZ* β-galactosidase: Structure and function of an enzyme of historical and molecular biological importance. *Protein Science* **21**, 1792–1807 (2012).

43. Bickers, S. C., Sayewich, J. S. & Kanelis, V. Intrinsically disordered regions regulate the activities of ATP binding cassette transporters. *Biochimica et Biophysica Acta (BBA) - Biomembranes* **1862**, 183202 (2020).

44. Kassem, N., Kassem, M. M., Pedersen, S. F., Pedersen, P. A. & Kragelund, B. B. Yeast recombinant production of intact human membrane proteins with long intrinsically disordered intracellular regions for structural studies. *Biochimica et Biophysica Acta (BBA) - Biomembranes* **1862**, 183272 (2020).

45. Ravindran, R. & Michnick, S. W. Biomolecular condensates as drivers of membrane trafficking and remodelling. *Current Opinion in Cell Biology* **89**, 102393 (2024).

46. Neidhardt, F. C., Bloch, P. L. & Smith, D. F. Culture Medium for Enterobacteria. *J Bacteriol* **119**, 736–747 (1974).

47. MembraneEnzymology. MembraneEnzymology/smdm: SMdM analysis in Escherichia coli cytoplasm. [https://doi.org/10.5281/ZENODO.5911836 (2022)].

48. MembraneEnzymology. MembraneEnzymology/PALM_Reconstruction: PALM Reconstruction v1.0. [https://doi.org/10.5281/ZENODO.14334015 (2024)].

49. McDONALD, K. L. & Webb, R. I. Freeze substitution in 3 hours or less: FREEZE SUBSTIUTION IN 3 HOURS OR LESS. *Journal of Microscopy* **243**, 227–233 (2011).

50. Abramson, J. *et al.* Accurate structure prediction of biomolecular interactions with AlphaFold 3. *Nature* **630**, 493–500 (2024).

51. Abraham, M. *et al.* GROMACS 2024.3 Manual. [https://doi.org/10.5281/ZENODO.13457083 (2024) doi:10.5281/ZENODO.13457083].

52. Abraham, M. J. *et al.* GROMACS: High performance molecular simulations through multi-level parallelism from laptops to supercomputers. *SoftwareX* **1–2**, 19–25 (2015).

53. Souza, P. C. T. *et al.* Martini 3: a general purpose force field for coarse-grained molecular dynamics. *Nat Methods* **18**, 382–388 (2021).

54. Kroon, P. *et al.* Martinize2 and Vermouth: Unified Framework for Topology Generation. Preprint at [https://doi.org/10.7554/eLife.90627.2 (2024)].

55. Kumar, H. *et al.* Lactose permease complex with thiodigalactoside and nanobody 9043: 6vbg. [https://doi.org/10.2210/pdb6vbg/pdb (2020)].

56. Smirnova, I., Kasho, V., Sugihara, J. & Kaback, H. R. Opening the periplasmic cavity in lactose permease is the limiting step for sugar binding. *Proc. Natl. Acad. Sci. U.S.A.* **108**, 15147–15151 (2011).

57. Drozdetskiy, A., Cole, C., Procter, J. & Barton, G. J. JPred4: a protein secondary structure prediction server. *Nucleic Acids Res* **43**, W389–W394 (2015).

58. Ruff, K. M. & Pappu, R. V. AlphaFold and Implications for Intrinsically Disordered Proteins. *Journal of Molecular Biology* **433**, 167208 (2021).

59. Wang, L., Brasnett, C., Borges-Araújo, L., Souza, P. C. T. & Marrink, S. J. Martini3-IDP: improved Martini 3 force field for disordered proteins. *Nat Commun* **16**, 2874 (2025).

60. Westendorp, M. S. S., Stevens, J. A., Bruininks, B. M. H. & Marrink, S.-J. Bentopy: building molecular dynamics simulations with cellular complexity and scale. [https://doi.org/10.5281/ZENODO.13818758 (2024)].

61. Wassenaar, T. A., Ingólfsson, H. I., Böckmann, R. A., Tieleman, D. P. & Marrink, S. J. Computational Lipidomics with *insane* : A Versatile Tool for Generating Custom Membranes for Molecular Simulations. *J. Chem. Theory Comput.* **11**, 2144–2155 (2015).

62. Pogozheva, I. D. *et al.* Comparative Molecular Dynamics Simulation Studies of Realistic Eukaryotic, Prokaryotic, and Archaeal Membranes. *J. Chem. Inf. Model.* **62**, 1036–1051 (2022).

63. De Jong, D. H., Baoukina, S., Ingólfsson, H. I. & Marrink, S. J. Martini straight: Boosting performance using a shorter cutoff and GPUs. *Computer Physics Communications* **199**, 1–7 (2016).

64. Kim, H., Fábián, B. & Hummer, G. Neighbor List Artifacts in Molecular Dynamics Simulations. *J. Chem. Theory Comput.* **19**, 8919–8929 (2023).

65. Gowers, R. *et al.* MDAnalysis: A Python Package for the Rapid Analysis of Molecular Dynamics Simulations. in 98–105 (Austin, Texas, 2016). doi:10.25080/Majora-629e541a-00e.

66. Michaud-Agrawal, N., Denning, E. J., Woolf, T. B. & Beckstein, O. MDAnalysis: A toolkit for the analysis of molecular dynamics simulations. *J Comput Chem* **32**, 2319–2327 (2011).

67. Humphrey, W., Dalke, A. & Schulten, K. VMD: Visual molecular dynamics. *Journal of Molecular Graphics* **14**, 33–38 (1996).

68. Hunter, J. D. Matplotlib: A 2D Graphics Environment. *Comput. Sci. Eng.* **9**, 90–95 (2007).

69. Baba, T. *et al.* Construction of *Escherichia coli* K-12 in-frame, single-gene knockout mutants: the Keio collection. *Molecular Systems Biology* **2**, 2006.0008 (2006).

70. Hanahan, D. Studies on transformation of Escherichia coli with plasmids. *Journal of Molecular Biology* **166**, 557–580 (1983).

71. Linnik, D. *et al*. Structural and functional implications of phase separation of membrane protein LacY in *Escherichia coli*. DataverseNL [https://doi.org/10.34894/X8GI6H (2026)]

72. Stevens, J. A. & Marrink, S. Simulation data: Structural and functional implications of phase separation of membrane protein LacY in in *Escherichia coli*. [https://doi.org/10.5281/ZENODO.17335657 (2026)].

Acknowledgements

We would like to thank Lyan van der Sleen for data discussions, José Vila Chã Losa and Matthias Heinemann for *E. coli* LY177 and BW25113 *ΔlacY* and Jelmer Coenradij for purified TrxA-mEos3.2 protein. The work of Dmitrii Linnik, Jan A. Stevens, Siewert-Jan Marrink and Bert Poolman was funded by the NWO National Science Program "The limits to growth" (grant number NWA.1292.19.170). Additionally, the work of Bert Poolman was supported by the NWO Gravitation program "Building a synthetic cell" (BaSyC). Ivan Maslov thanks the European Union for funding his research under the HORIZON TMA MSCA Postdoctoral Fellowships action (project MemProDx, 101149735).

Authors contributions

D.L. and **S.S** cloned and expressed the genes. **D.L., S.S.** and **I.M.** performed wide-field fluorescence microscopy and FRAP measurements. **D.L.** performed SMdM and confocal measurements. **D.L.** performed experiments with nucleoid degradation, division inhibition and spheroplasts formation. **J.A.S.** performed the MD simulations. **G.K.S-W** performed ^{14}C-lactose uptake experiments and SDS-PAGE. **R.de.B.** performed high-pressure freezing and transmission electron microscopy. **C.M.P.** provided IT supervision and helped **D.L.** with analysis methods development. **D.L.** and **B.P.** conceptualized the project. **D.L.**, **I.M.**, **J.A.S, S.J.M** and **B.P**. analyzed and discussed the data. Manuscript was written by **D.L., I.M.** and **B.P.** with contribution from all authors.

Competing Interests Statement

The authors declare no competing interests.

Table 1. List of *E. coli* strain used in the work.

Name	Plasmid	Purpose	Source / Reference
BW25113	-	Expression of genes, protein production	69
DH5α	-	Storage of plasmids	70
BW25113 *ΔlacY*	-	Deletion of lactose permease gene	69
LY177	-	MG1655 derivative with inducible nucleoid degradation	25
DH5α pACYC LacY	pACYC_LacY-mEos3.2	Source of *lacY* gene and pACYC vector	30
DH5α PopZ-eGFP	pMA-RQ_popZ-mRuby	Source of *popZ* and *mRuby* genes	22
DH5α mEos3.2	pBAD_mEos3.2	Source of *mEos3.2* gene and pBAD vector	21
BW25113 LacY^{mEos}	pBAD_LacY-mEos3.2	Expression of LacY-mEos3.2 fusion for visualization	This work
BW25113 LacY$^{mEos-Pop}$	pBAD_LacY-mEos3.2-PopTag	Expression of LacY-mEos3.2 fusion for visualization	This work
BW25113 *ΔlacY* LacY^{mEos}	pBAD_LacY-mEos3.2	Expression of LacY for lactose uptake experimetns	This work
BW25113 *ΔlacY* LacY$^{mEos-Pop}$	pBAD_LacY-mEos3.2-PopTag	Expression of LacY-PopTag for lactose uptake experimetns	This work
LY177 LacY^{mEos}	pSN1 pAYCY_LacY-mEos3.2	LacY-mEos3.2 fusion visualization in cells with degraded nucleoid	This work
LY177 LacY$^{mEos-Pop}$	pSN1 pAYCY_LacY-mEos3.2-PopTag	LacY-mEos3.2-PopTag fusion for visualization of cells with degraded nucleoid	This work
BW25113 LacY^{mEos}-LacZ^{mRuby}	pBAD_LacY-mEos3.2 pACYC_LacZ-mRuby	Expression of LacY-mEos3.2 and LacZ-mRuby fusions for visualization	This work
BW25113 LacY$^{mEos-Pop}$-LacZ^{mRuby}	pBAD_LacY-mEos3.2-PopTag pACYC_LacZ-mRuby	Expression of LacY-mEos3.2-PopTag and LacZ-mRuby fusions for visualization	This work
BW25113 LacY^{mEos}-LacZ$^{mRuby-Pop}$	pBAD_LacY-mEos3.2 pACYC_LacZ-mRuby-PopTag	Expression of LacY-mEos3.2 and LacZ-mRuby-PopTag fusions for visualization	This work
BW25113 LacY$^{mEos-Pop}$-LacZ$^{mRuby-Pop}$	pBAD_LacY-mEos3.2-PopTag pACYC_LacZ-mRuby-PopTag	Expression of LacY-mEos3.2-PopTag and LacZ-mRuby-PopTag fusions for visualization	This work
BW25113 *ΔlacY* LacY-LacZ	pBAD_LacY pACYC_LacZ	Expression of LacY and LacZ proteins for functional tests	This work
BW25113 *ΔlacY* LacY^{Pop}-LacZ	pBAD_LacY-PopTag pACYC_LacZ	Expression of LacY-PopTag and LacZ proteins for activity assays	This work
BW25113 *ΔlacY* LacY-LacZ^{Pop}	pBAD_LacY pACYC_LacZ-PopTag	Expression of LacY and LacZ-PopTag proteins for activity assays	This work
BW25113 *ΔlacY* LacY^{Pop}-LacZ^{Pop}	pBAD_LacY-PopTag pACYC_LacZ-PopTag	Expression of LacY-PopTag and LacZ-PopTag proteins for activity assays	This work

Figure 1. Localization and mobility of LacY^{mEos} and LacY$^{mEos-Pop}$ in *E. coli*. (**a**) Wide-field fluorescence microscopy images of LacY-mEos3.2 and LacY-mEos3.2-PopTag proteins in *E. coli* BW25113. **(b)** PALM reconstruction of LacY-mEos3.2-PopTag in representative live and fixed cells. Left column: 100,000 frames of acquisition were used for super-resolution reconstruction; right panel: 20.000 frames of the same acquisition. Color bars indicate intensity of the reconstructed images, which directly corresponds to localization counts. Scale bars are 1 µm. **(c)** Fraction of protein localizations at the cell poles (20% of cell length) for BW25113 LacY^{mEos} and BW25113 LacY$^{mEos-Pop}$ strains, calculated from single-molecule localization microscopy. Data presented and mean ± SEM, averaged over 23 and 13 cells for BW25113 LacY^{mEos} and BW25113 LacY$^{mEos-Pop}$, respectively. **(d)** Fluorescence recovery profiles of cells expressing LacY$^{mEos-Pop}$. The cell pole (number of bleached areas n=20), lateral membrane (n=25) or full cell (n=23) were bleached and the intensity recovery over time was measured. Fluorescence recovery at the pole was also measured (n=17) upon treatment of the cells with chloramphenicol. Data from at least 3 biological replicates is shown as mean ± SEM. **(e)** Fluorescence recovery profiles of cells expressing LacY^{mEos}. The cell pole was bleached (number of bleached poles in different cells n=21). Data from at least 3 biological replicates is shown as mean ± SEM. **(f)** Diffusion maps of *E. coli* BW25113 LacY$^{mEos-Pop}$ (top) and BW25113 LacY^{mEos} (bottom), reconstructed by fitting displacements starting in each 100 nm pixel bin with equation 3. **(g)** Apparent diffusion coefficients of LacY$^{mEos-Pop}$ and LacY^{mEos} measured at the cell poles (20% of cell length) and lateral membrane. 23 and 21 cells were measured for BW25113 LacY$^{mEos-Pop}$ and BW25113 LacY^{mEos} strains, respectively, and data are presented as mean ± SEM. Two-sided t-test used for pairwise data comparison. **(h)** Transmission electron microscopy images of 100 nm thin sections of *E. coli* BW25113 LacY^{mEos} and BW25113 LacY$^{mEos-Pop}$. Orange arrows are pointing at the edges of electron-dense regions at the cytoplasmic face of the inner membrane. Scale bars are 200 nm. Significance levels are presented as asterisk signs: (ns) for $p>0.05$, (***) for $p<0.001$ and (****) for $p<0.0001$. Exact p-values are presented in the Supplementary Figure 4. Source data are provided as a Source Data file.

Figure 2. Molecular dynamics simulations show PopTag-mediated clustering of LacY membrane proteins. (a) Comparison of clustering behavior between LacY (top) and LacY^{Pop} (bottom) proteins embedded in lipid membranes. Initial frames (left) show the start configuration of the simulation, while the end frames (right) show the final protein organization after 50 µs**. (b)** Representative snapshot from the PopTag condensate simulation, with helices colored (helix 1 in red, helix 2 in blue, helix 3 in green). **(c)** Contact map analysis comparing inter-PopTag interactions when fused to membrane-embedded LacY (left) versus in a solution-mediated condensate (right). The hydrophobicity profile (far left) illustrates the amphipathic nature of PopTag's helices, with helix 1 (orange box) showing highest interaction frequency in both environments. **(d)** Quantitative

analysis of clustering dynamics showing the probability distribution of protein cluster numbers during the last 2.5 μs of simulations (**left**) and the time evolution of protein-protein contacts throughout a representative 50 μs trajectory (**right**) for LacY^{Pop} (teal) and LacY (purple). Protein-protein contacts were determined per protein rather than per individual residue, where two proteins are considered in contact when they share at least one residue-residue interaction. Source data are provided as a Source Data file.

Figure 3. Perturbation of nucleoid and shape of *E. coli* reveals curvature-dependent LacY$^{mEos\text{-}Pop}$ distribution. (a) and **(b)** Wide-field fluorescence microscopy images of *E. coli* BW25113 LacY^{mEos} and BW25113 LacY$^{mEos\text{-}Pop}$, treated with cephalexin for **(a)** 4 h and **(b)** 7 h. Homogeneous distribution of LacY-mEos3.2 and predominantly polar localization of LacY-mEos3.2-PopTag is observed in all conditions. To visualize the nucleoid, cells were stained with 15 μM DAPI before the acquisition. Scale bars are 3 μm for 4-hour treated and 5 μm for 7-hour treated cells. **(c)** Wide-field fluorescence microscopy images of *E. coli* LY177 LacY^{mEos} and LY177 LacY$^{mEos\text{-}Pop}$. Left panel: cells not producing the *I-SceI* endonuclease. Right panel: cells producing *I-SceI* endonuclease. Degradation of nucleoid was confirmed by DAPI staining. The brightness of the mEos3.2 and DAPI channels was adjusted to the same levels for left and right panels. Scale bars are 3 μm. **(d)** Wide-field fluorescence microscopy images of spheroplasts formed from *E. coli* BW25113 LacY^{mEos} and BW25113 LacY$^{mEos\text{-}Pop}$. BW25113 LacY$^{mEos\text{-}Pop}$ cells were measured immediately after spheroplast formation and after 30 min incubation at room temperature. Scale bars are 3 μm. The dynamic redistribution of phase-separated LacY$^{mEos\text{-}Pop}$ over approximately 30 min can be seen in Supplementary Video 1. **(e)** Wide-field fluorescence microscopy images of LacY$^{mEos\text{-}Pop}$ distribution in hyperosmotically stressed spheroplasts after 30 min of incubation with 0.5 M NaCl. LacY-mEos3.2-PopTag is no longer homogeneously distributed and forms clusters at membrane regions with curvature. Scale bars are 3 μm.

Figure 4. LacY activity outside and inside biomolecular condensates. (a) ^{14}C-lactose uptake by *E. coli* BW25113 *ΔlacY* LacY^{mEos} and BW25113 *ΔlacY* LacY$^{mEos\text{-}Pop}$. Data were fitted with an exponential plateau equation and U_{MAX} is the plateau value of the fit. R^2 for the fits of BW25113 *ΔlacY* LacY^{mEos} and BW25113 *ΔlacY* LacY$^{mEos\text{-}Pop}$, are 0.97 and 0.95, respectively. Data from 3 biological replicates are presented as mean ± SEM, n = 7 independent experiments. **(b)** Box plots of U_{MAX} of ^{14}C-lactose uptake by BW25113 *ΔlacY* LacY^{mEos} and BW25113 *ΔlacY* LacY$^{mEos\text{-}Pop}$. Data are presented as a best-fit value and a standard error of the fit of the data from panel a. Extra sum-of-squares F-test used to compare the best-fit values. **(c)** ^{14}C-lactose uptake curves of BW25113 *ΔlacY* LacY^{mEos} and BW25113 *ΔlacY* LacY$^{mEos\text{-}Pop}$ cells after osmotic upshift. Cells grown in 275 mOsmol were upshifted with 160 mM NaCl or 320 mM NaCl, resulting in medium osmolarities of 545 and 881 mOsmol, respectively. Data are presented as mean ± SEM, n = 7 independent experiments (from 3 biological replicates) for 275 mOsmol and 4 independent experiments (from 2 biological replicates) for 545 and 881 mOsmol. **(d)** Left panel – box plots of

U_{MAX} of ^{14}C-lactose uptake by *E. coli* BW25113 *ΔlacY* LacY^{mEos} and BW25113 *ΔlacY* LacY$^{mEos\text{-}Pop}$ after osmotic upshift. Data are presented as a best-fit value and a standard error of the fit of the data from panel c. Extra sum-of-squares F-test used to compare the best-fit values. Right panel – table of U_{max} parameters for all measured conditions. **(e)** Wide-field fluorescence microscopy images of *E. coli* BW25113 *ΔlacY* LacY^{mEos} and BW25113 *ΔlacY* LacY$^{mEos\text{-}Pop}$ after osmotic upshift from 275 to 545 and 881 mOsmol. 5-times zoom-ins show severely deformed *E. coli* BW25113 *ΔlacY* LacY. Significance levels are presented as asterisk signs: (ns) for p>0.05, (*) for p<0.05 and (**) for p<0.0101. Exact p-values are presented in the Supplementary Figure 4. Source data are provided as a Source Data file.

Figure 5. LacY^{Pop} and LacZ^{Pop} heterocondensates *in vivo*. (a) Confocal laser-scanning microscopy of *E. coli* BW25113 LacY^{mEos}-LacZ^{mRuby}, BW25113 LacY$^{mEos\text{-}Pop}$-LacZ^{mRuby}, BW25113 LacY^{mEos}-LacZ$^{mRuby\text{-}Pop}$ and BW25113 LacY$^{mEos\text{-}Pop}$-LacZ$^{mRuby\text{-}Pop}$, co-expressing PopTag and non-PopTag versions of membrane LacY^{mEos} and cytoplasmic LacZ^{mRuby} proteins. (I) and (II) are pointing to cells with different scenarios of LacY$^{mEos\text{-}Pop}$– LacZ$^{mRuby\text{-}Pop}$ interaction (described in the main text). Scale bars are 5 μm. **(b)** Transmission electron microscopy images of 100 nm thin sections of BW25113 LacY$^{mEos\text{-}Pop}$-LacZ$^{mRuby\text{-}Pop}$ cells showing scenarios I and II. A dashed orange line outlines the apparent electron-dense regions. Panel **a** highlights cells with scenarios I and II, which are enlarged in the insets of panel **b**. **(c)** *In vivo* β-galactosidase activity (in arbitrary units) in *E. coli* BW25113 ΔlacY LacY LacZ, BW25113 ΔlacY LacY^{Pop}-LacZ, BW25113 ΔlacY LacY-LacZ^{Pop} and BW25113 ΔlacY LacY^{Pop}-LacZ^{Pop}. The β-MUG conversion rate (Supplementary Figure 12) was corrected for the amount of protein, determined by fluorescent imaging of SDS-PAGE gels (Supplementary Figure 13) and normalized to the activity in BW25113 *ΔlacY* LacY LacZ strain; referred to in the figure as adjusted LacZ activity. Data are presented as a best-fit slope value and a standard error of the linear fit of the data presented on the Supplementary Figure 12. Source data are provided as a Source Data file.

Figure 6. Model of curvature-driven localization of membrane-anchored biomolecular condensates. **(a)** Localization pattern of LacY-mEos3.2-PopTag condensates (green) in rod-shaped *E. coli*. Light grey color represents cytoplasm, dark grey – periplasm, yellow line is inner membrane, and orange is nucleoid. LacY-mEos3.2-PopTag in the lateral membrane does not create large phase-separated condensates as the local PopTag concentration is limited by the surface-to-volume ratio. Only some small and dynamic condensates are formed. The smaller cytoplasmic volume for the same surface area (higher surface-to-volume ratio) at the cell pole results in a higher concentration of PopTags, which favors condensate formation. **(b)** Pre-membrane volume at 10, 30 and 50 nm thickness as a function of membrane radius (300 nm → infinity). The decrease in pre-membrane volume is 3.4, 10.7 and 18.7 % for a thickness of 10, 30 and 50 nm, respectively. **(c)** Schematic representation of membrane-anchored biomolecular condensate and heterocondensate. Approximate distance from the membrane is based on EM

data and structures of LacY, LacZ and fluorescent proteins. One layer of $LacZ^{mRuby\text{-}Pop}$ condensate on top of $LacY^{mEos\text{-}Pop}$ has a maximal predicted thickness of ~30 nm and two layers of $LacZ^{mRuby\text{-}Pop}$ yield ~50 nm.

Editor's Summary

Phase-separation of the transport protein LacY alters its membrane localization and mobility, preserves its transport activity, reduces cell membrane stress under osmotic upshift, and LacY forms mixed condensates with the enzyme β-galactosidase LacZ.

Peer review information: *Nature Communications* thanks the anonymous reviewers for their contribution to the peer review of this work. A peer review file is available.

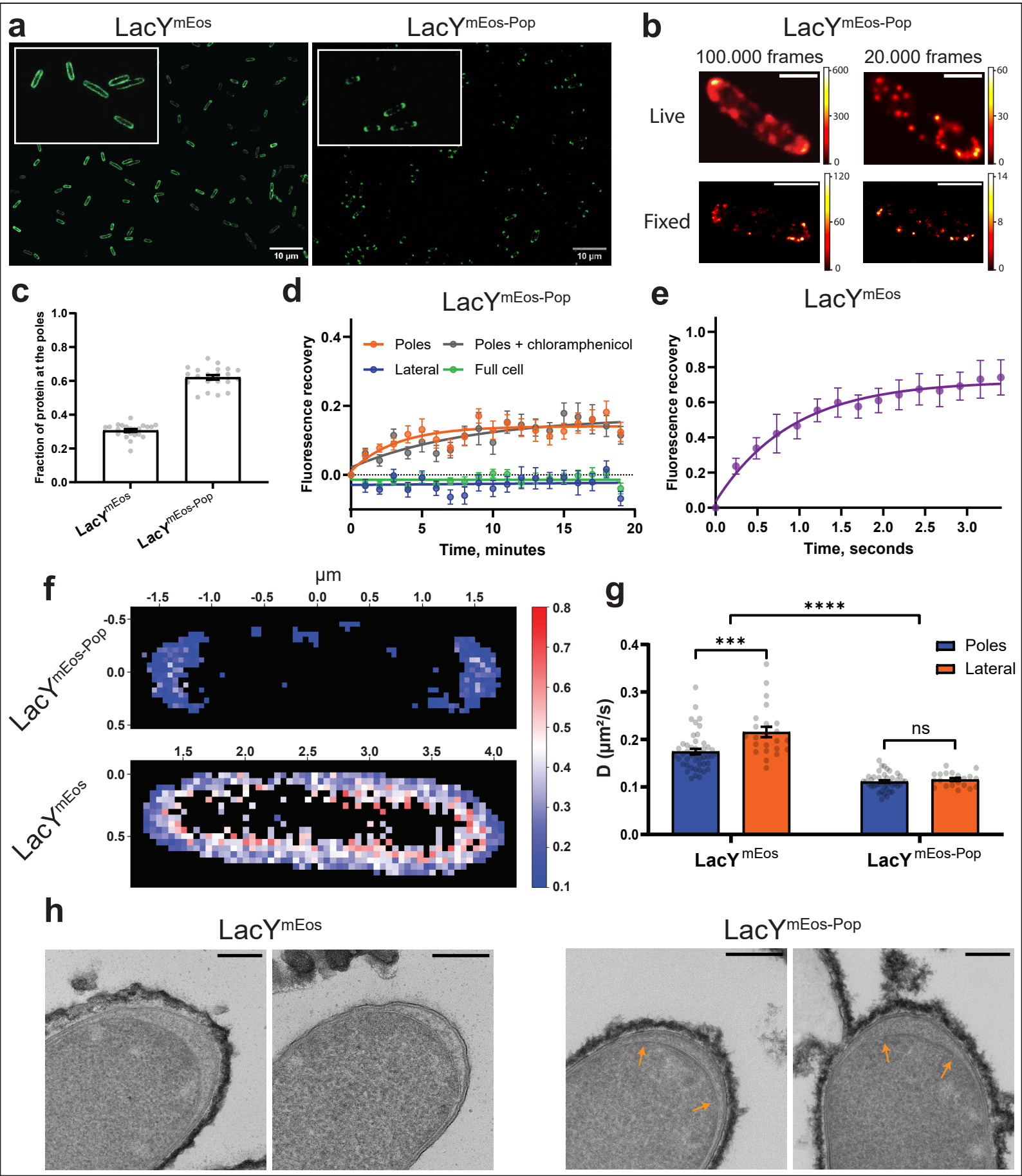
a
LacY^mEos
LacY^mEos-Pop
10 µm
10 µm
b
LacY^mEos-Pop
100.000 frames
20.000 frames
Live
Fixed
600
300
0
60
30
0
120
60
0
14
8
0
c
Fraction of protein at the poles
1.0
0.8
0.6
0.4
0.2
0.0
LacY^mEos
LacY^mEos-Pop
d
LacY^mEos-Pop
Fluoresecnce recovery
0.4
0.2
0.0
Poles
Poles + chloramphenicol
Lateral
Full cell
0
5
10
15
20
Time, minutes
e
LacY^mEos
Fluorescence recovery
1.0
0.8
0.6
0.4
0.2
0.0
0.0
0.5
1.0
1.5
2.0
2.5
3.0
Time, seconds
f
µm
-1.5
-1.0
-0.5
0.0
0.5
1.0
1.5
LacY^mEos-Pop
-0.5
0.0
0.5
1.5
2.0
2.5
3.0
3.5
4.0
LacY^mEos
0.0
0.5
0.8
0.7
0.6
0.5
0.4
0.3
0.2
0.1
g
****
***
ns
Poles
Lateral
D (µm²/s)
0.4
0.3
0.2
0.1
0.0
LacY^mEos
LacY^mEos-Pop
h
LacY^mEos
LacY^mEos-Pop

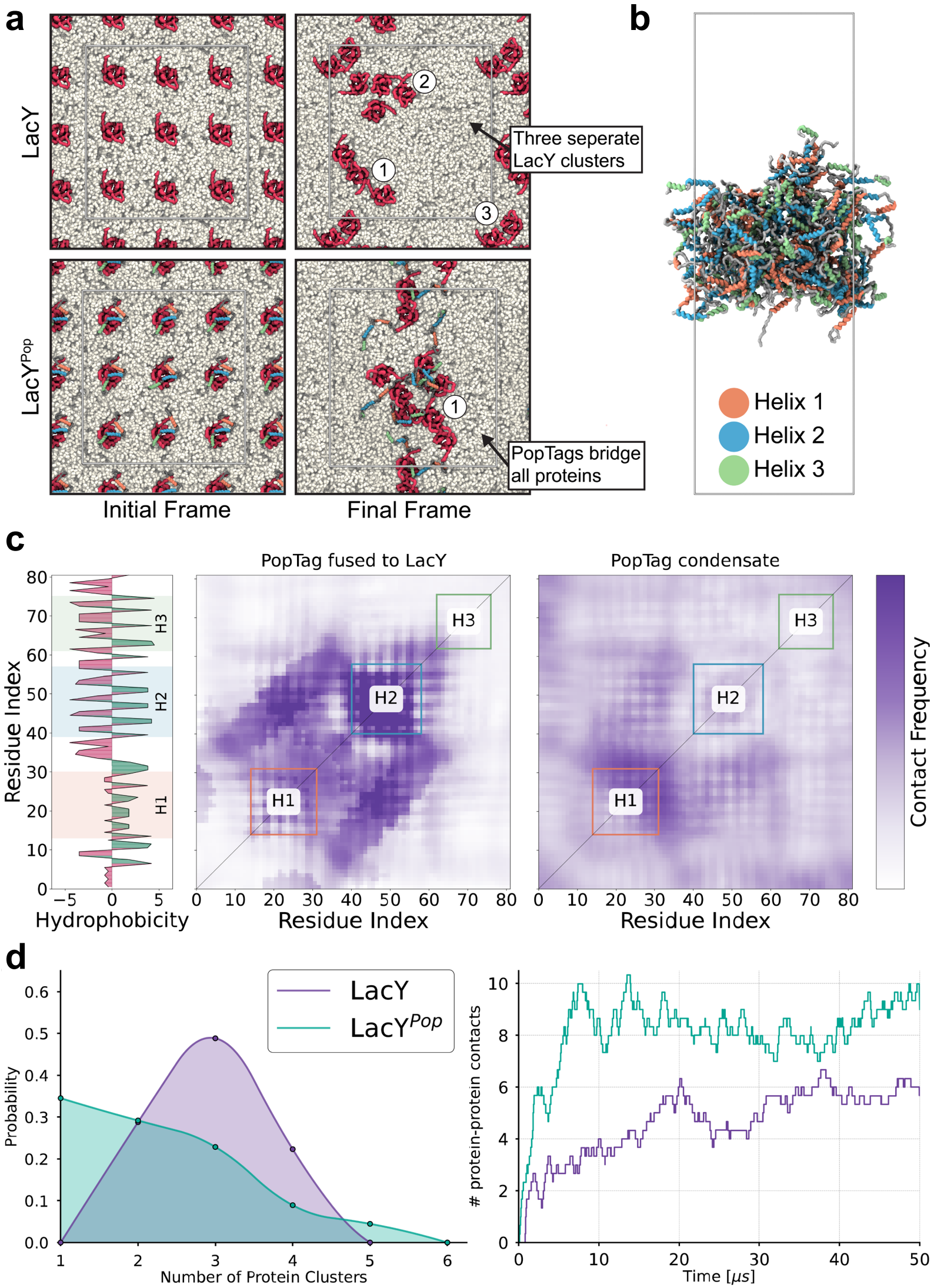
a
LacY
LacY^Pop
Three seperate LacY clusters
PopTags bridge all proteins
Initial Frame
Final Frame
b
Helix 1
Helix 2
Helix 3
c
PopTag fused to LacY
PopTag condensate
Residue Index
Hydrophobicity
H1
H2
H3
Contact Frequency
d
LacY
LacY^Pop
Probability
Number of Protein Clusters
protein-protein contacts
Time [μs]

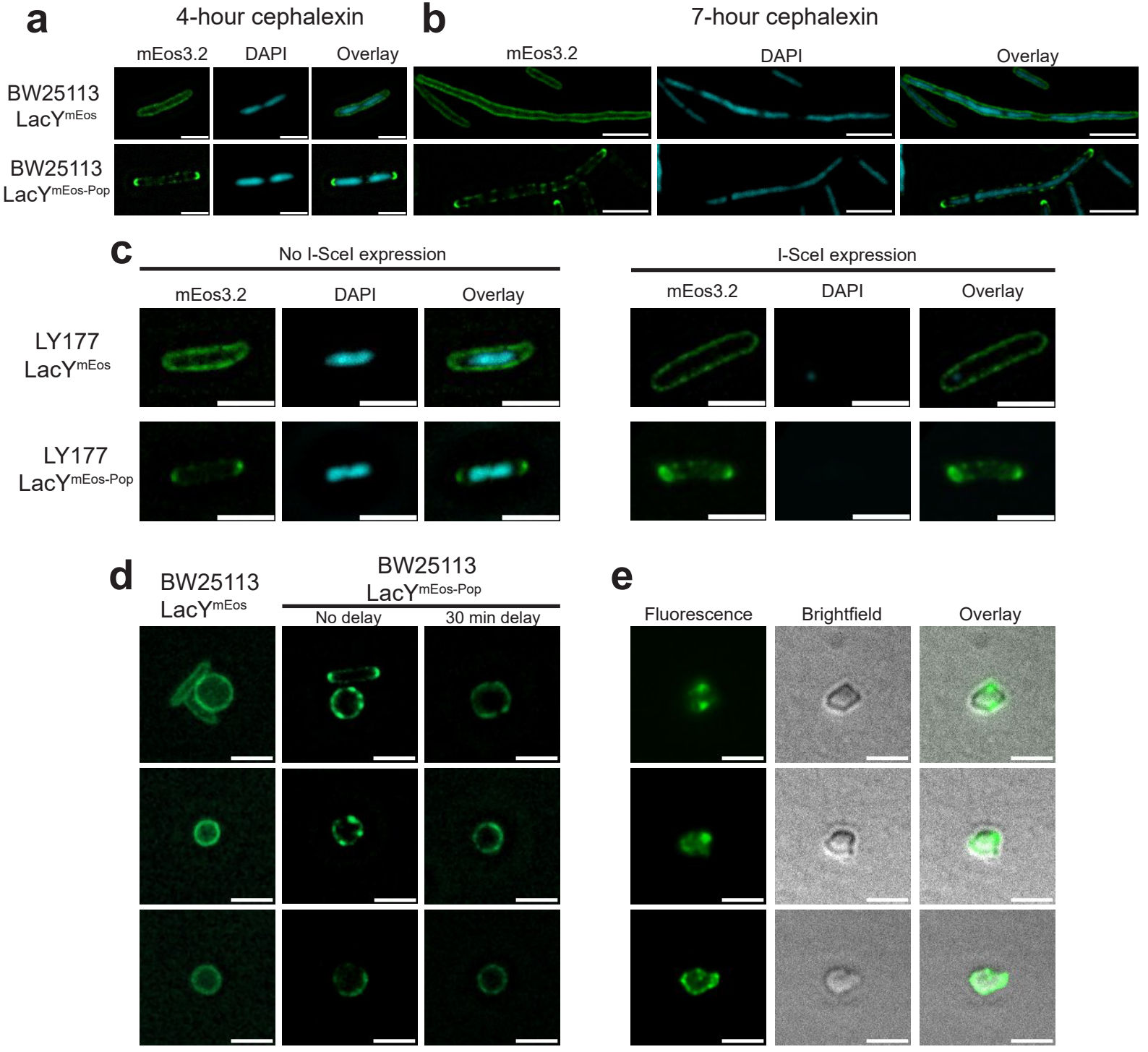
a
4-hour cephalexin
mEos3.2
DAPI
Overlay
BW25113 LacY^mEos
BW25113 LacY^mEos-Pop
b
7-hour cephalexin
mEos3.2
DAPI
Overlay
c
No I-SceI expression
I-SceI expression
mEos3.2
DAPI
Overlay
LY177 LacY^mEos
LY177 LacY^mEos-Pop
d
BW25113 LacY^mEos
BW25113 LacY^mEos-Pop
No delay
30 min delay
e
Fluorescence
Brightfield
Overlay

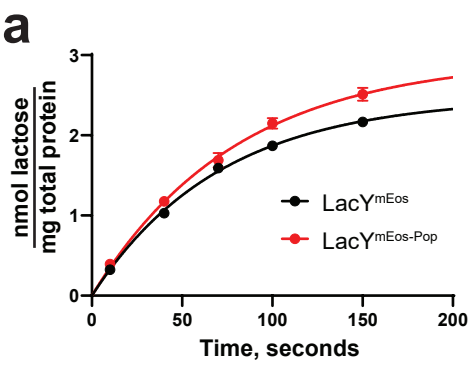

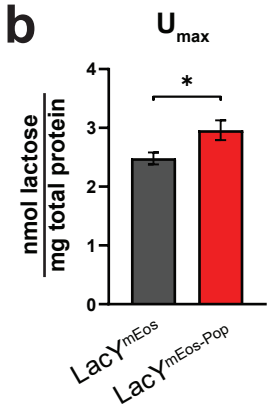

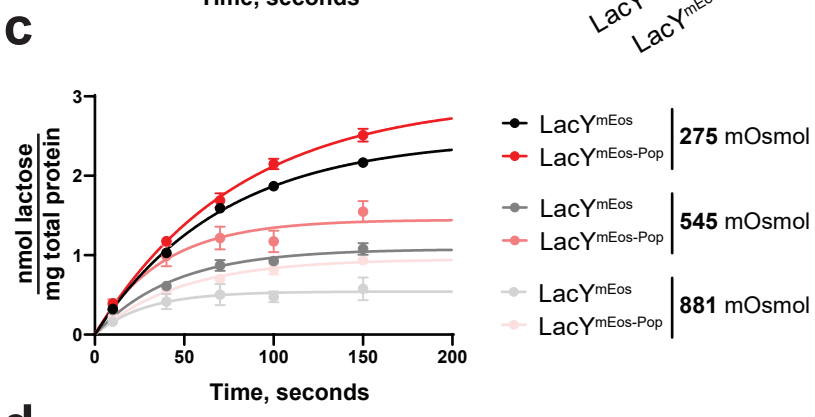

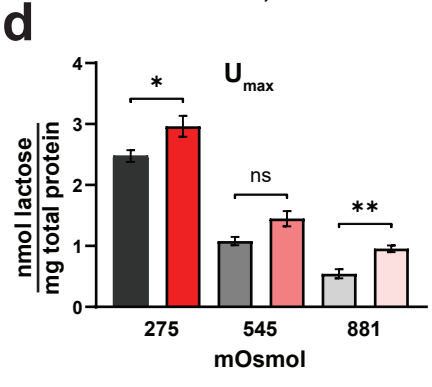

U_{max}

LacY^{mEos}	LacY$^{mEos\text{-}Pop}$	
2.48 ± 0.09	2.96 ± 0.17	**275** mOsmol
1.08 ± 0.07	1.45 ± 0.13	**545** mOsmol
0.54 ± 0.08	0.95 ± 0.06	**881** mOsmol

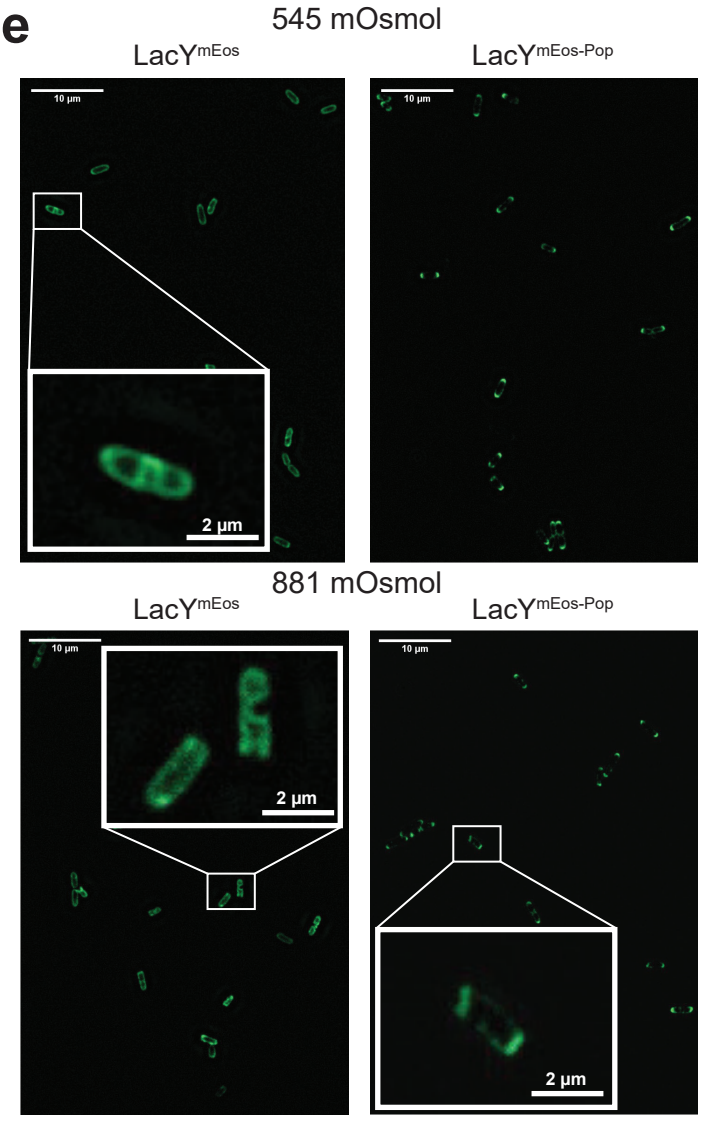

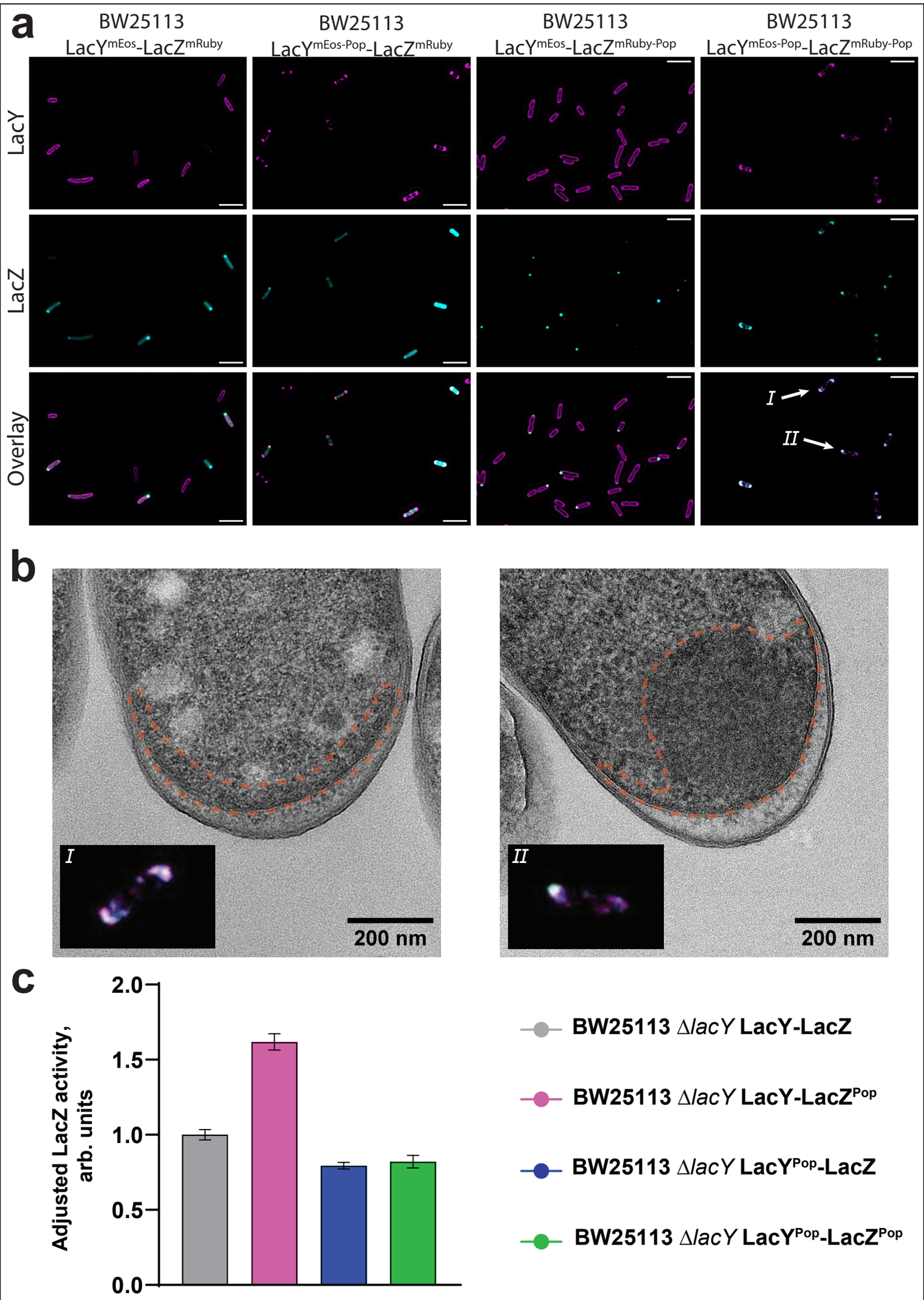
a
BW25113 LacY^mEos-LacZ^mRuby
BW25113 LacY^mEos-Pop-LacZ^mRuby
BW25113 LacY^mEos-LacZ^mRuby-Pop
BW25113 LacY^mEos-Pop-LacZ^mRuby-Pop
LacY
LacZ
Overlay
I
II
b
I
II
200 nm
200 nm
c
Adjusted LacZ activity, arb. units
2.0
1.5
1.0
0.5
0.0
BW25113 ΔlacY LacY-LacZ
BW25113 ΔlacY LacY-LacZ^Pop
BW25113 ΔlacY LacY^Pop-LacZ
BW25113 ΔlacY LacY^Pop-LacZ^Pop

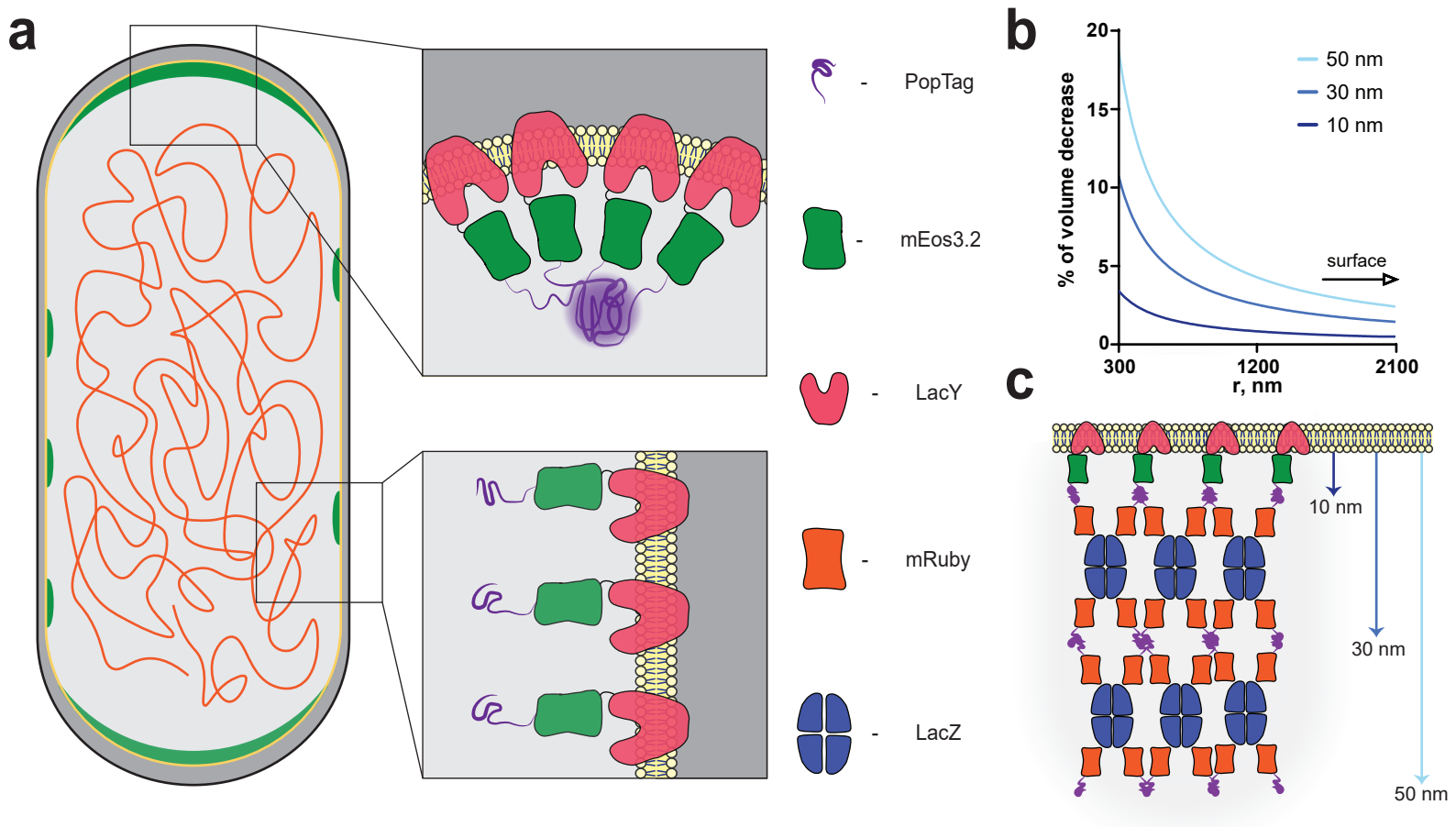
a
PopTag
mEos3.2
LacY
mRuby
LacZ
b
% of volume decrease
20
15
10
5
0
300
1200
2100
r, nm
50 nm
30 nm
10 nm
surface
c
10 nm
30 nm
50 nm